Clays and Clay Minerals (2025), **73**, e17, 1–21
doi:10.1017/cmn.2024.42

Original Paper

Evidence for partially chloritized smectite in Gale crater, Mars

Elizabeth B. Rampe[1]*, Valerie M. Tu[2], Richard V. Morris[1], Joanna V. Clark[2], Thomas F. Bristow[3], Bethany L. Ehlmann[4], Sarah Perry[5], Venus Cruz[6], Brandon Rasmussen[4], Douglas W. Ming[1] and P. Douglas ArcherJr.[7]

[1]NASA Johnson Space Center, Houston, TX 77058, USA; [2]Texas State University – Amentum JETS II Contract at NASA Johnson Space Center, Houston, TX 77058, USA; [3]NASA Ames Research Center, Mountain View, CA 94043, USA; [4]California Institute of Technology, Pasadena, CA 91125, USA; [5]California Department of Water Resources, Sacramento, CA 95814, USA; [6]University of Nevada, Las Vegas, Las Vegas, NV 89154, USA and [7]Amentum at NASA JSC, Houston, TX 77058, USA

Abstract

Characterizing the structure and composition of clay minerals on the surface of Mars is important for reconstructing past aqueous processes and environments. Data from the CheMin X-ray diffraction (XRD) instrument on the Mars Science Laboratory *Curiosity* rover demonstrate a ubiquitous presence of collapsed smectite (basal spacing of 10 Å) in ~3.6-billion-year-old lacustrine mudstone in Gale crater, except for expanded smectite (basal spacing of 13.5 Å) at the base of the stratigraphic section in a location called Yellowknife Bay. Hypotheses to explain expanded smectite include partial chloritization by $Mg(OH)_2$ or solvation-shell H_2O molecules associated with interlayer Mg^{2+}. The objective of this work is to test these hypotheses by measuring partially chloritized and Mg-saturated smectite using laboratory instruments that are analogous to those on Mars rovers and orbiters. This work presents Mars-analog XRD, evolved gas analysis (EGA), and visible/shortwave-infrared (VSWIR) data from three smectite standards that were Mg-saturated and partially and fully chloritized with $Mg(OH)_2$. Laboratory data are compared with XRD and EGA data collected from Yellowknife Bay by the *Curiosity* rover to examine whether the expanded smectite can be explained by partial chloritization and what this implies about the diagenetic history of Gale crater. Spectral signatures of partial chloritization by hydroxy-Mg are investigated that may allow the identification of partially chloritized smectite in Martian VSWIR reflectance spectra collected from orbit or *in situ* by the SuperCam instrument suite on the Mars 2020 *Perseverance* rover. Laboratory XRD and EGA data of partially chloritized saponite are consistent with data collected from *Curiosity*. The presence of partially chloritized (with $Mg(OH)_2$) saponite in Gale crater suggests brief interactions between diagenetic alkaline Mg^{2+}-bearing fluids and some of the mudstone exposed at Yellowknife Bay, but not in other parts of the stratigraphic section. The location of Yellowknife Bay at the base of the stratigraphic section may explain the presence of alkaline Mg^{2+}-bearing fluids here but not in other areas of Gale crater investigated by *Curiosity*. Early diagenetic fluids may have had a sufficiently long residence time in a closed system to equilibrate with basaltic minerals, creating an elevated pH, whereas diagenetic environments higher in the section may have been in an open system, therefore preventing fluid pH from becoming alkaline.

Keywords: *Curiosity*; diagenesis; Mars; partially chloritized smectite; smectite

(Received: 03 April 2024; revised: 07 October 2024; accepted: 20 November 2024)

Introduction

Phyllosilicates are an important mineral group in ancient (~3.5–4.1 Ga, based on impact crater counting) Martian strata because they are indicative of water–rock interactions and can help constrain aqueous conditions that may have been habitable by microbial life. Orbital visible/shortwave-infrared (VSWIR) reflectance data collected by the Observatoire pour la Mineralogie, l'Eau, les Glaces et l'Activité (OMEGA), and the Compact Reconnaissance Imaging Spectrometer for Mars (CRISM) indicate that smectite is the most common phyllosilicate group on the Martian surface, and Fe/Mg-smectite (e.g. nontronite and saponite) is much more common than Al-smectite (e.g. montmorillonite) (e.g. Poulet et al., 2005; Mustard et al., 2008; Ehlmann et al., 2011). The types and diversity of phyllosilicates, however, depend on the geologic environment, where phyllosilicates in igneous settings are dominated by Fe/Mg-smectite and chlorite, and phyllosilicates in sedimentary rocks and stratigraphic sections generally contain a mix of Fe/Mg-smectite and

Corresponding author: E.B. Rampe; Email: elizabeth.b.rampe@nasa.gov
Cite this article: Rampe E.B., Tu V.M., Morris R.V., Clark J.V., Bristow T.F., Ehlmann B.L., Perry S., Cruz V., Rasmussen B., Ming D.W., & Archer P.D.Jr. (2025). Evidence for partially chloritized smectite in Gale crater, Mars. *Clays and Clay Minerals* **73**, e17, 1–21. https://doi.org/10.1017/cmn.2024.42

Al-phyllosilicates (e.g. montmorillonite and kaolinite) (Ehlmann et al., 2011; Ehlmann et al., 2013).

Smectite has been identified in abundances of up to ~30 wt.% in early Hesperian-aged (~3.6 Ga old) lacustrine mudstone in Gale crater by the CheMin X-ray diffractometer on the Mars Science Laboratory *Curiosity* rover (e.g. Vaniman et al., 2014; Bristow et al., 2018; Rampe et al., 2020a; Tu et al., 2021; Thorpe et al., 2022). The composition and structure of the smectite identified in Gale crater changes throughout a 400+ m vertical stratigraphic succession of fluvial-lacustrine deposits. Trioctahedral Fe^{3+}-bearing saponite, from oxidation of Fe^{2+} in the octahedral site, is present at the base of the section (Treiman et al., 2014). Mixed dioctahedral/trioctahedral smectite is present in the middle of the section, and fully dioctahedral nontronite is present in the Glen Torridon region (Bristow et al., 2018; Bristow et al., 2021; Tu et al., 2021; Thorpe et al., 2022). All phyllosilicates measured by CheMin have a broad basal peak at ~10 Å and relatively low K_2O content, indicating the presence of collapsed smectite as opposed to illite (e.g. Bristow et al., 2018), except for one sample at the base of the stratigraphic section. This sample, named 'Cumberland', was drilled from a formation called Yellowknife Bay and has a clearly defined basal spacing of 13.5 Å (Vaniman et al., 2014) (Fig. 1). This peak position remained constant for >150 Martian days in the warm and dry environment within the CheMin instrument, indicating that the phyllosilicate did not collapse from dehydration over time.

Constraining the composition and structure of phyllosilicates on the Martian surface permits the characterization of aqueous environments in which they formed and development of a more complete geologic history of the planet. Fe/Mg-smectite commonly forms from mafic parent material, which is abundant on Mars. The abundant Fe/Mg-smectites on Mars probably formed from a variety of processes, including magmatic processes (e.g. deuteric alteration), hydrothermalism, metamorphism, precipitation in lake sediments, surficial weathering profiles, and, perhaps, under a steamy primordial atmosphere (e.g. Ehlmann et al., 2013; Cannon et al., 2017; Mangold et al., 2019). Al-phyllosilicates, like montmorillonite and kaolinite, are more common in pedogenic and open-system weathering environments where leaching removes basic cations (e.g. Meunier, 2005; Ehlmann et al., 2013). Chlorite is indicative of diagenesis or metamorphism, but chlorite can also form in pedogenic environments (e.g. Barnhisel and Bertsch, 1989; Meunier, 2005).

Smectite can be partially or fully chloritized in soil environments on Earth. Partially chloritized smectite (also known as hydroxy-interlayered smectite) typically forms through the replacement of solvated cations in smectite interlayer sites by hydroxy-Al, -Mg, or -Fe polymeric components (Barnhisel and Bertsch, 1989). Hydroxy-Al smectite is more common on Earth than hydroxy-Fe or hydroxy-Mg smectite because Al is more abundant in the Earth's crust than Fe and Mg. It forms under moderately acidic pH, low organic content, frequent wetting and drying cycles, and oxidizing conditions. Mg- and Fe-partially chloritized smectite have been identified on Earth in alkaline, saline lake sediments (Jones and Weir, 1983) and reducing sedimentary environments (Lynn and Whittig, 1966), respectively. Partially chloritized smectite is structurally similar to mixed-layer chlorite-smectite. Mixed-layer chlorite-smectite is composed of complete chlorite and smectite layers stacked on top of one another in the *c* crystallographic direction. Partially chloritized smectite is smectite with incomplete gibbsite- or brucite-like sheets (or 'pillars' as they are sometimes referred to in the literature) in the interlayer site (Fig. 2), making partially chloritized smectite a type of incipient mixed-layer chlorite smectite. This interlayer structure allows the smectite to swell when treated with ethylene glycol but prevents it from fully collapsing when heated to 500°C (Barnhisel and Bertsch, 1989).

Bristow et al. (2015) hypothesized that the expanded smectite in Yellowknife Bay could be explained by partial chloritization by hydroxy-Mg. This idea is supported by the identification of Mg-rich diagenetic features in Yellowknife Bay (Léveillé et al., 2014). Furthermore, mafic silicate minerals, olivine and pyroxene, are abundant across the Martian surface because Mars is dominated by basalt and sediments derived from basalt (e.g. Rogers and Christensen, 2007). As such, aqueous alteration on Mars results in more Mg^{2+}, Fe^{2+}, and Fe^{3+} in solution than is typically seen in continental terrestrial settings (e.g. Hurowitz and McLennan, 2006). The Mars science community has previously lacked the data necessary to identify partially chloritized smectite on the Martian surface. The objective of this work was to further interpret the clay mineralogy of Gale crater to learn more about past aqueous environments. This work tested the hypothesis that expanded smectite in Yellowknife Bay is a result of partial chloritization by hydroxy-Mg, by measuring partially chloritized and Mg-saturated smectite using laboratory instruments that are analogous to those on Mars rovers and orbiters. Laboratory data are compared with data collected by instruments on the *Curiosity* rover to look for signatures of partial chloritization in Martian data.

Methods

Partial chloritization procedure

The samples studied were nontronite (sample NAu-2 from the Source Clay Repository of The Clay Minerals Society), montmorillonite (Source Clay SWy-1), and Fe-saponite (a Mars-analog smectite sourced from Griffith Park, California (Treiman et al., 2014), abbreviated to 'GP' here). The samples were selected as starting materials for partial chloritization experiments. The <2 μm size fraction of all samples was separated via centrifugation. Na-saturation (Moore and Reynolds, 1997) was performed prior to partial chloritization to start with a homogeneous interlayer composition. Each smectite was Mg-saturated (Moore and Reynolds, 1997) to provide a comparison to data from chloritized smectite. Mg-saturation was performed by distributing clay in a 0.1 M $MgCl_2$ solution in an ultrasonicator for 2 min, and then shaking for 24 h. Clay suspensions were centrifuged, replenished with 0.1 M $MgCl_2$ twice more, and then washed with deionized water and a 50:50 by volume mixture of deionized water and ethanol. Mg-saturated smectites were allowed to dry at 60°C for 24 h (Moore and Reynolds, 1997).

Portions of the Mg-saturated smectite samples were chloritized with $Mg(OH)_2$ as the 'pillars' in the interlayer site at various OH:Mg molar ratios to achieve various levels of chloritization. Molar OH:Mg ratios of 0.5, 1.0, 1.5, and 1.75 in the solution were chosen to mimic previous partial chloritization methods (Xeidakis, 1996). Increasing the OH:Mg ratio causes more $Mg(OH)_2$ pillars to precipitate in the interlayer site, resulting in a greater degree of chloritization. Briefly, a clay suspension was made by adding ~0.8 g Mg-saturated smectite in 50 mL milli-Q water, and 1.5 M NaOH was added dropwise to desired OH:Mg molar ratios of 0.5, 1.0, 1.5, or 1.75. The clay suspension was stirred vigorously during titration, and the final product was centrifuged, washed twice with deionized H_2O to remove soluble salts, and dried at 25°C.

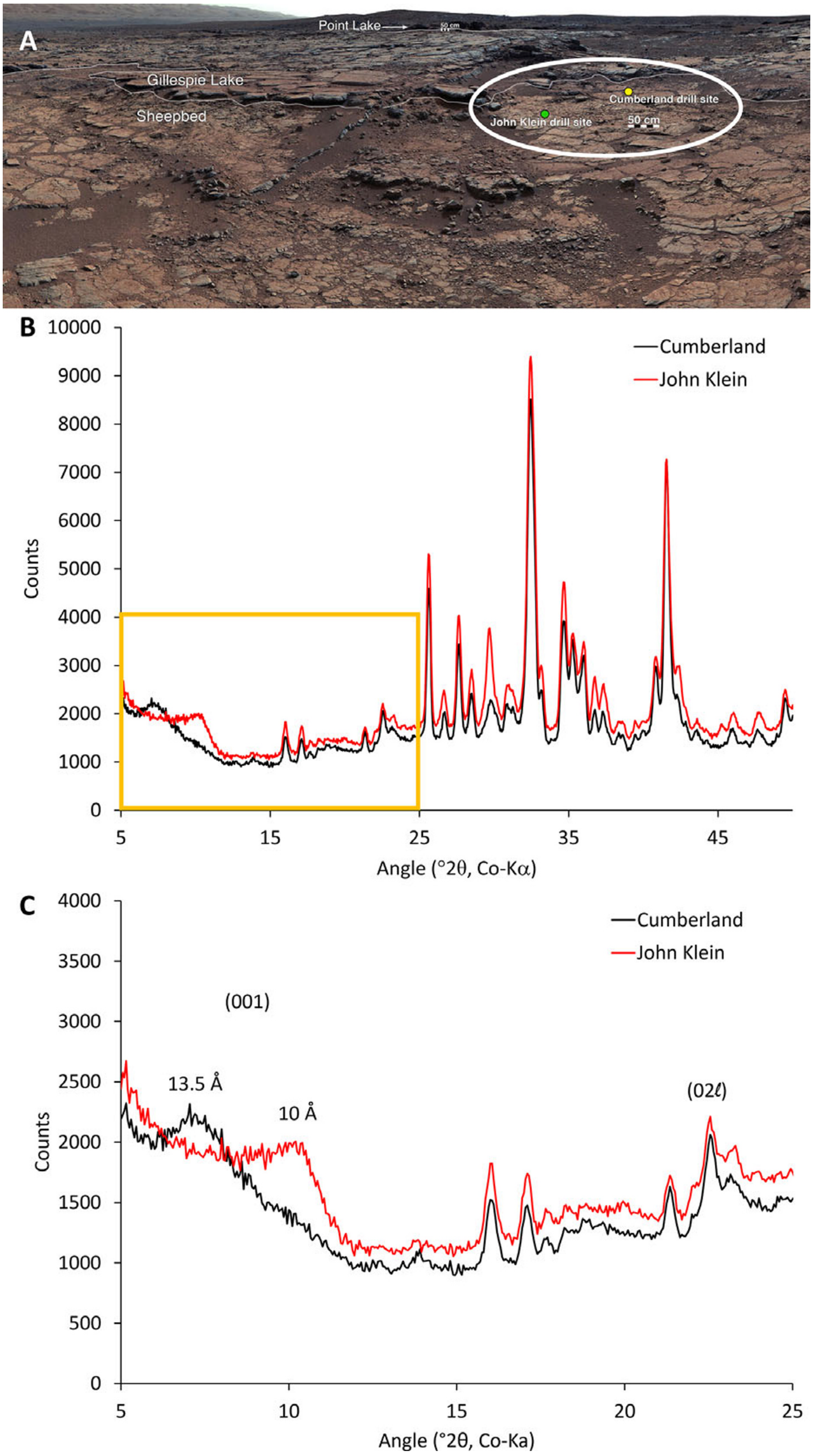

Figure 1. Yellowknife Bay drill site and CheMin data. (A) Mastcam mosaic of Yellowknife Bay with the geologic members and drill sites identified. Image credit: NASA/JPL/MSSS. (B) CheMin X-ray diffraction patterns of the John Klein and Cumberland drill targets. (C) Portion of John Klein and Cumberland CheMin XRD patterns showing the positions of (001) and (02*l*) peaks.

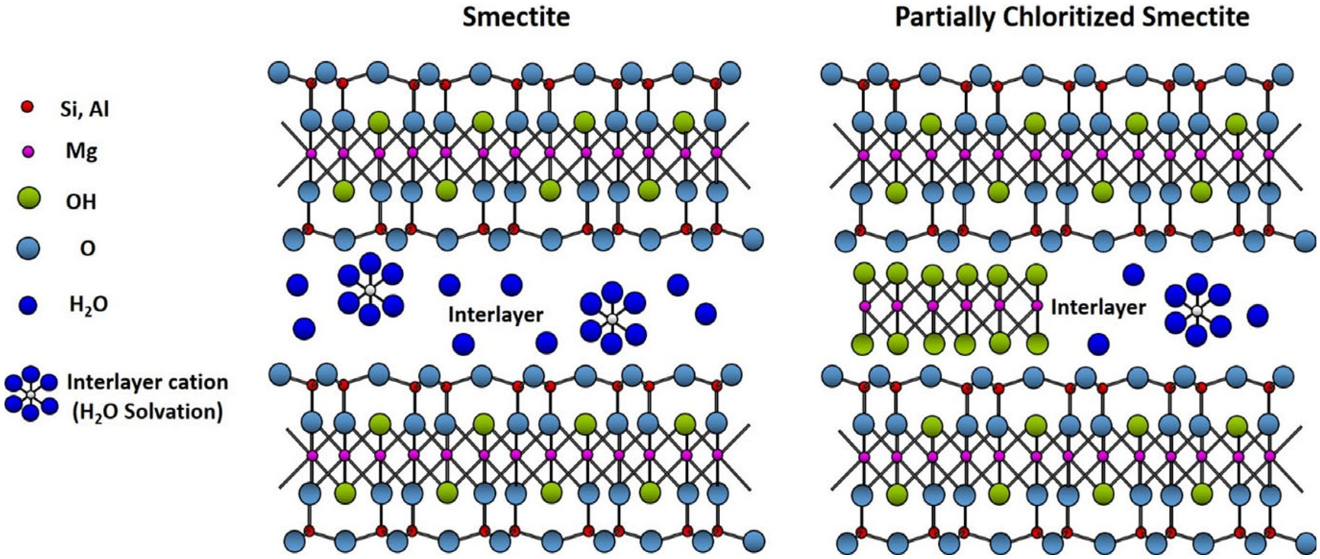

Figure 2. Structural diagram of smectite and partially chloritized smectite. Left: diagram of saponite, a trioctahedral smectite, showing water molecules and solvated cations in the interlayer site; right: diagram of partially chloritized saponite, showing water molecules, solvated cations, and short domains of brucite sheets in the interlayer site.

X-ray diffraction

Random powder mounts of Mg-saturated and $Mg(OH)_2$ chloritized smectite samples were analyzed at ~1% (in dry $N_{2(g)}$) and ~90% relative humidity (RH) on a non-ambient Anton Paar stage in a Panalytical X'Pert Pro MPD X-ray diffractometer at the NASA Johnson Space Center (JSC) from 2 to 80°2θ (CoKα), with a 0.02°2θ step size, and 10 s $step^{-1}$. The samples were held at the desired RH for at least 2 h before analysis. Random powder mounts, rather than oriented mounts, were measured because these are most analogous to the patterns measured by the CheMin instrument. Mg-saturated and chloritized samples were measured on a CheMin IV XRD instrument, a laboratory analog to the CheMin instrument on board *Curiosity*. Mg-saturated nontronite was measured using an Olympus Terra instrument because the CheMin IV was not in operation. Samples were heated under desiccating conditions in $N_{2(g)}$ at 200°C (i.e. 'heat desiccated') prior to analysis to drive off interlayer water and emulate the low hydration state of smectite on the Martian surface. CheMin IV measurements were made with dry $N_{2(g)}$ flowing over the samples. Unlike most laboratory X-ray diffractometers, CheMin IV operates in transmission mode, and data are collected from 4 to 55°2θ (Co-Kα) with a 0.05° step size (e.g. Blake et al., 2012). CheMin uses a cobalt X-ray source to minimize fluorescence from Fe. Terra is a field-portable version of CheMin with the similar X-ray source, angular range and resolution, geometry, and sample handling system as CheMin (e.g. Sarrazin et al., 2008). Peak positions were calculated as the centroid position from Lorentz-polarization (LP)-corrected patterns using the Materials Data Inc. *JADE* program.

Thermal and evolved gas analysis

Mg-saturated and chloritized smectite samples were analyzed individually using a Setaram Labsys EVO thermal gravimeter (TG)/differential scanning calorimeter (DSC)/furnace connected to a Pfeiffer ThermoStar quadrupole mass spectrometer (QMS) at JSC configured to operate similarly to the Sample Analysis at Mars-Evolved Gas Analysis (SAM-EGA) instrument on board the *Curiosity* rover (e.g. Mahaffy et al., 2012). EGA measures and quantifies the gases evolved during pyrolysis of a sample. TG/DSC data show sample weight loss and exothermic/endothermic reactions, respectively, during sample heating. Although the SAM instrument does not have TG/DSC capabilities, they are used in this study to better understand chemical reactions and phase transitions in the Mg-saturated and chloritized smectite. Samples of ~10 mg were placed in alumina ceramic crucibles. Sample and identical empty crucibles were placed inside the furnace, which was then purged with He gas and set to a pressure of 30 mbar and a flow rate of 10 standard cubic centimeters per minute (sccm). The crucibles were heated from ~30 to 1000°C at a heating rate of 35°C min^{-1}. All samples were run in duplicate. EGA data from mass-to-charge ratios (m/z) of 2–100 were collected and mass-normalized, but only the results from m/z=18 (i.e. H_2O) are presented here because it is specifically the water-release data that can be used to identify specific phyllosilicates (e.g. McAdam et al., 2020).

Visible/shortwave infrared (VSWIR) reflectance spectroscopy

VSWIR reflectance spectra (0.35–2.5 μm) were acquired at JSC on Mg-saturated and chloritized smectite samples with Analytical Spectral Devices (ASD) FieldSpec3 Hi-Res fiber optic spectrometers configured with Mug lights. Samples were measured under ambient laboratory conditions, after desiccation at 25°C in a glove box purged with dry $N_{2(g)}$ (~150–400 parts per million by volume (ppmv), H_2O, or 0.5–2% RH), and after heating to 200°C under dry $N_{2(g)}$. Samples were desiccated in the dry $N_{2(g)}$ glove box at 25°C and were heated to 200°C under $N_{2(g)}$. Samples were held at each temperature until the spectra showed no changes (22–96 h for samples at 25°C and 24–384 h for samples at 200°C). For many Mg-saturated samples, there was insufficient material to exclude contributions from the sample substrate from the measured reflectance. The substrate material (LEE Filters Black Foil 280) has no absorptions relevant to the analysis but is dark, ~4% reflectance over the full range of the ASD instrument.

Results

This section describes the XRD patterns, EGA traces, and VSWIR spectra of the Mg-saturated and chloritized smectite samples. The

Table 1. LP-corrected d_{001} and d_{002} for Mg-saturated and chloritized smectite samples measured on the Panalytical at 90% RH and ~1% RH and heat-desiccated samples measured on the CheMin IV under dry $N_{2(g)}$

	Panalytical 90% RH		Panalytical dry $N_{2(g)}$		CheMin IV (heat desiccation, dry $N_{2(g)}$)	
Sample ID	001 peak	002 peak	001 peak	002 peak	001 peak	002 peak
GP Mg-saturated	15.4	—	13.8	—	9.9	—
GP OH:Mg 0.5	15.0	7.4	13.9	7.2	12.2	—
GP OH:Mg 1.0	14.3	7.3	13.9	7.3	13.6	7.4
GP OH:Mg 1.5	14.6	7.3	14.1	7.3	13.6	7.4
GP OH:Mg 1.75	14.6	7.3	13.9	7.3	13.8	7.3
NAu-2 Mg saturated	15.5	—	13.9	—	12.9*	—
NAu-2 OH:Mg 0.5	13.7	—	13.9	—	9.7	—
NAu-2 OH: Mg 1.0	14.4	7.4	14.2	7.3	14.1	7.4
NAu-2 OH:Mg 1.5	14.5	7.3	14.3	7.4	14.3	7.4
NAu-2 OH:Mg 1.75	14.5	7.4	14.4	7.4	14.3	7.3
SWy-1, Mg saturated	15.3	—	13.8	—	13.9	—
SWy-1 OH:Mg 0.5	15.8	—	13.0	—	9.8	—
SWy-1 OH:Mg 1.0	13.5	—	13.6	—	12.9	—
SWy-1 OH:Mg 1.5	14.9	7.7	14.0	7.7	14.1	7.7
SWy-1 OH:Mg 1.75	14.7	7.5	14.3	7.5	14.4	7.5

Peak positions were measured using the centroid. Values are reported in Å. *NAu-2 measurements were made on an Olympus Terra instrument.

results are separated by smectite type (i.e. Griffith Park saponite, NAu-2 nontronite, and SWy-1 montmorillonite). The results focus on: (1) the position of the (001) peaks in XRD patterns for comparison with the (001) peak in the Cumberland sample drilled on Mars; (2) the temperatures at which H_2O was released in EGA for comparison with SAM EGA traces in Cumberland; and (3) changes in VSWIR spectra with increasing degree of chloritization.

X-ray diffraction

For all three smectites, partial chloritization led to changes to the (001) peak positions and no changes to the (02*l*) and (06*l*) peaks (Table 1; see also Table S1 in the Supplementary material), demonstrating that the chloritization procedure did not disrupt the *b*-axis of the smectite crystal structure. For each set of patterns measured under different conditions, a broad peak at ~7.4 Å appeared when smectite standards were subject to chloritization. The appearance of the (002) peak is a result of changes to the layer structure factor of smectites (e.g. Moore and Reynolds, 1997) as $Mg(OH)_2$ layers replace exchangeable interlayer sites. As described in more detail below, an increase in OH:Mg ratio in the chloritization procedure generally caused an increase in (002) height intensity to the (001) intensity (i.e. a decrease in the (001)/(002) intensity ratio), indicating a greater degree of chloritization with increase in OH:Mg ratio. The measured positions of the (001) peaks typically showed that complete chloritization was achieved with OH:Mg=1.5 and 1.75.

Griffith Park saponite

In all XRD measurements, the GP saponite has a (02*l*) peak at ~4.60 Å and a (06*l*) peak position of ~1.53 Å (Fig. 3; see also Table S1 and Fig. S3 in the Supplementary material), consistent with trioctahedral smectite (e.g. Brindley, 1952; Moore and Reynolds, 1997; Vaniman et al., 2014). For samples measured at 90% RH on the Panalytical XRD, the Mg-saturated sample was the most expanded with a position of 15.4 Å, whereas the chloritized samples had d_{001}≈14.3–15.0 Å (Fig. 3A). When measured under $N_{2(g)}$ on the Panalytical, the Mg-saturated and chloritized samples had similar d_{001} values, from ~13.8 to 14.1 Å (Fig. 3B). Heat-desiccated samples measured under $N_{2(g)}$ on the CheMin IV showed that chloritized samples with greater OH:Mg ratios were the most expanded with d_{001}≈13.6–13.8 Å, the Mg-saturated sample is the least expanded with a d_{001} of 9.9 Å, and the least chloritized sample (OH:Mg=0.5) has an intermediate d_{001} of 12.2 Å (Fig. 3C). A weak, broad peak at ~4.9 Å is apparent in chloritized samples with OH:Mg=1.0, 1.5, and 1.75 in all patterns measured on the Panalytical and CheMin IV. The position of this peak is consistent with a (003) reflection.

NAu-2 nontronite

All XRD patterns from NAu-2 have a (02l) peak at ~4.53 Å and a (06l) peak at ~1.51 Å (Fig. 4; see also Table S1 and Fig. S2 in the Supplementary material), which are diagnostic of dioctahedral smectite (e.g. Brindley, 1952; Moore and Reynolds, 1997; Vaniman et al., 2014). The Mg-saturated NAu-2 nontronite sample measured at 90% RH on the Panalytical was the most expanded with a (001) peak position of 15.4 Å, and the chloritized nontronite samples have smaller d_{001} at 13.7–14.5 Å (Fig. 4A). When measured under dry $N_{2(g)}$ on the Panalytical, the Mg-saturated NAu-2 sample has a very broad (001) peak with a maximum at 13.9 Å, suggesting a range of hydration states. The chloritized nontronite samples measured under $N_{2(g)}$ on the Panalytical show an increase in d_{001} with the increase in extent of chloritization, from 13.9 Å for OH:Mg=0.5 to 14.4 Å for

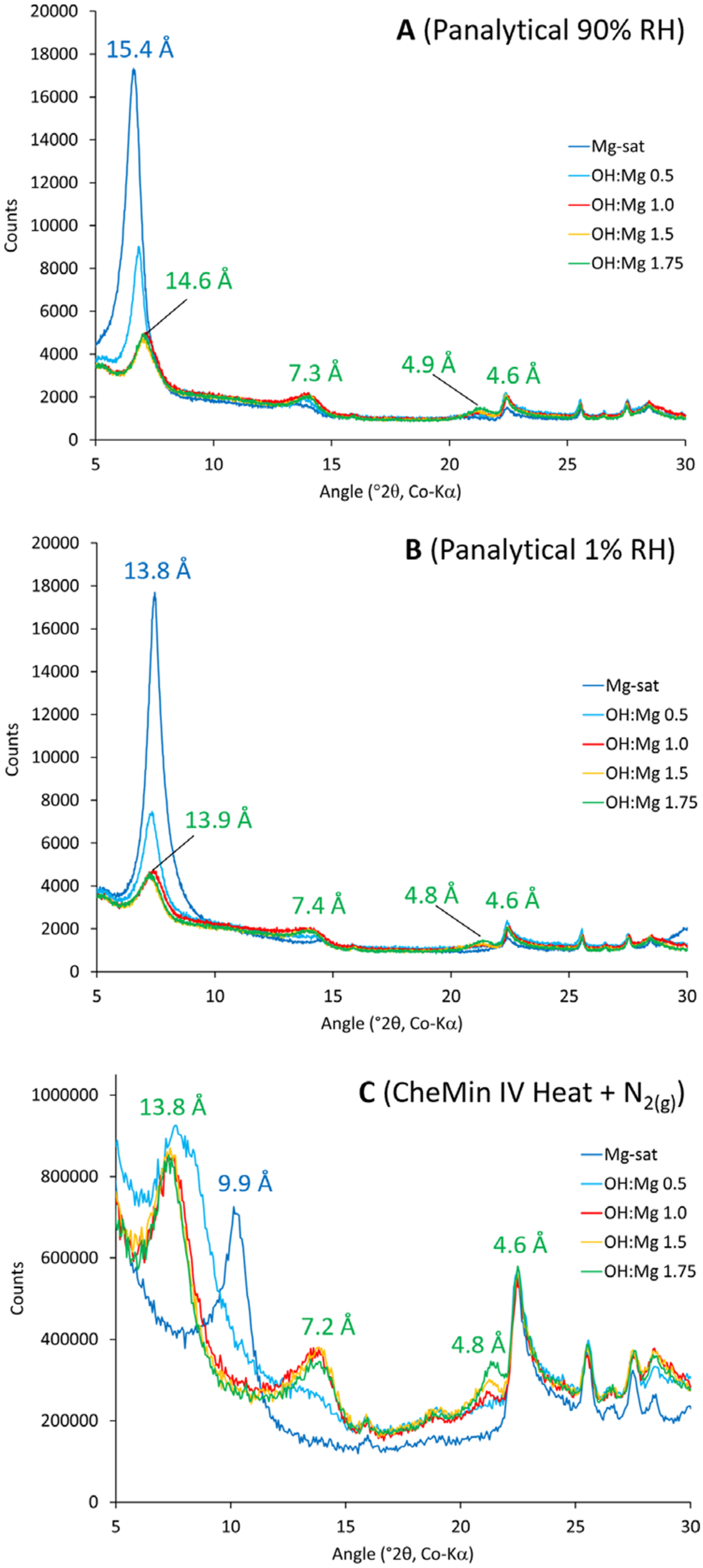

Figure 3. XRD patterns from 5 to 30°2θ (20.5 to 3.5 Å) of Mg-saturated and chloritized GP saponite. LP-corrected d_{001} of Mg-saturated samples and d_{001}, d_{002}, and d_{02l} of OH:Mg=1.75 samples are labeled for reference. (A) Patterns measured on the Panalytical at 90% RH. (B) Patterns measured on the Panalytical at ~1% RH (i.e. under dry $N_{2(g)}$). (C) Patterns of heat-treated samples measured on the CheMin IV under dry $N_{2(g)}$.

OH:Mg=1.75 (Fig. 4B). Heat-desiccated NAu-2 nontronite samples measured under $N_{2(g)}$ on the CheMin IV demonstrate that the chloritized samples with higher degrees of partial chloritization (i.e. higher OH:Mg ratios) have the largest basal spacings, and those with lower ratios have the smallest basal spacings (Fig. 4C). The OH:Mg=0.5 sample was the least expanded with a d_{001} of 9.7 Å,

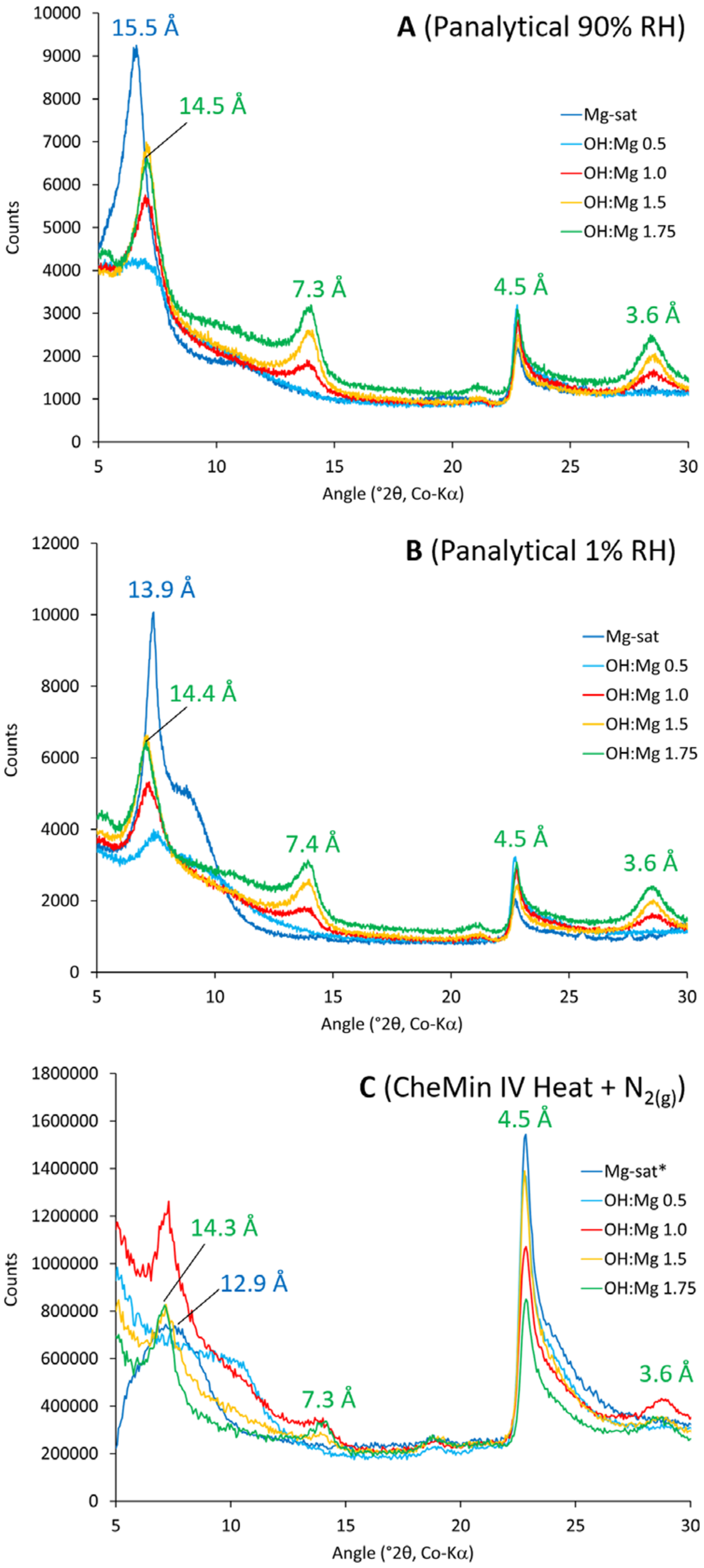

Figure 4. XRD patterns from 5 to 30°2θ (20.5 to 3.5 Å) of Mg-saturated and chloritized NAu-2 nontronite. LP-corrected d_{001} of Mg-saturated samples and d_{001}, d_{002}, d_{02l}, and d_{004} of OH:Mg=1.75 samples are labeled for reference. (A) Patterns measured on the Panalytical at 90% RH. (B) Patterns measured on the Panalytical at ~1% RH (i.e. under dry $N_{2(g)}$). (C) Patterns of heat-treated samples measured on the CheMin IV under dry $N_{2(g)}$. *The Mg-saturated sample was measured on a Terra instrument under ambient laboratory conditions after heat desiccation.

the OH:Mg=1 sample has a d_{001} of 14.1 Å, and the OH:Mg=1.5 and 1.75 samples had d_{001} of 14.3 Å. Chloritized samples with OH:Mg=1.0, 1.5, and 1.75 also had a peak at ~3.6 Å, consistent with the (004) reflection. The occurrence of this peak along with the (002) at ~7.3 Å demonstrates further a greater degree of chloritization.

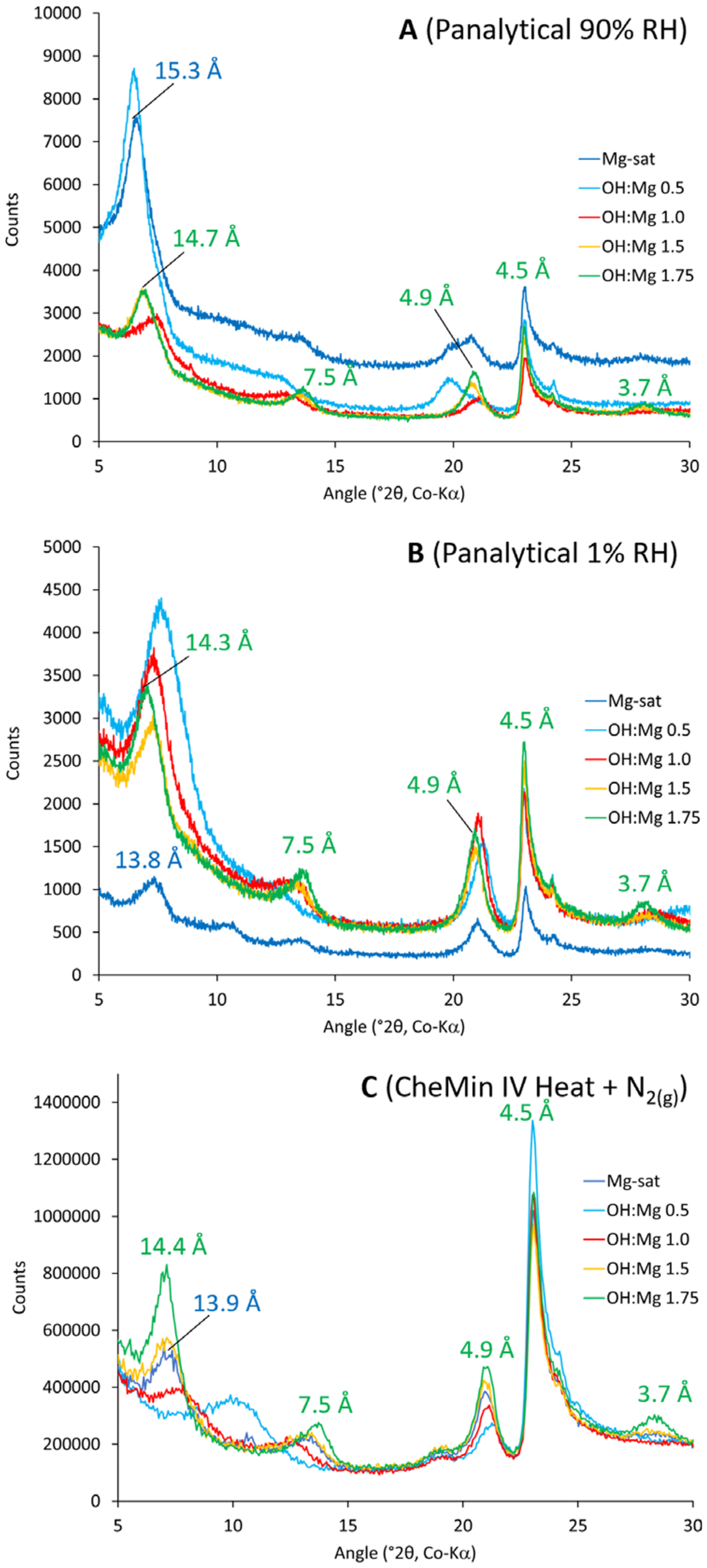

Figure 5. XRD patterns from 5 to 30°2θ (20.5 to 3.5 Å) of Mg-saturated and chloritized SWy-1 montmorillonite. LP-corrected d_{001} of Mg-saturated samples and d_{001}, d_{002}, d_{02l}, and d_{004} of OH:Mg=1.75 samples are labeled for reference. (A) Patterns measured on the Panalytical at 90% RH. (B) Patterns measured on the Panalytical at ~1% RH (i.e. under dry $N_{2(g)}$). (C) Patterns of heat-treated samples measured on the CheMin IV under dry $N_{2(g)}$.

SWy-1 montmorillonite

All SWy-1 samples have a (06*l*) peak at ~1.50 Å and a (02*l*) peak at ~4.48 Å (Fig. 5; see also Table S1 and Fig. S3 in the Supplementary material), which are diagnostic of dioctahedral smectite (e.g. Brindley, 1952; Moore and Reynolds, 1997; Vaniman et al., 2014). When measured at 90% RH, the OH:Mg=0.5 sample has the largest basal spacing with a d_{001} of 15.8 Å, followed by the Mg-saturated sample with a d_{001} of 15.3 Å (Fig. 5A). The chloritized samples with greater OH:Mg ratios have smaller basal spacings than the Mg-saturated sample, where the OH:Mg=1.0, 1.5, and 1.75 samples have d_{001} of 13.5, 14.9, and 14.7 Å, respectively. When measured under dry $N_{2(g)}$ on the Panalytical, Mg-saturated montmorillonite has a d_{001} of 13.8 Å, and the chloritized samples show an increase in d_{001} with an increase in chloritization, from 13.0 Å for the OH:Mg=0.5 sample up to 14.3 Å for the OH:Mg=1.75 sample (Fig. 5B). SWy-1 samples heat-desiccated and measured under $N_{2(g)}$ on CheMin IV have a large range of (001) peak positions. The Mg-saturated sample has a d_{001} at 13.9 Å, and, as for the samples measured under dry $N_{2(g)}$ on the Panalytical, the chloritized samples measured on the CheMin IV show an increase in d_{001} with increase in chloritization, from 9.8 Å for the OH:Mg=0.5 sample up to 14.4 Å for the OH:Mg=1.75 sample (Fig. 5C). A peak at ~4.9 Å is generally more pronounced in chloritized samples with OH:Mg=1.0, 1.5, and 1.75, but this peak is also present in Mg-saturated patterns. This is the (003) peak, which is higher in amplitude because of the lower octahedral Fe content of SWy-1 compared with the other

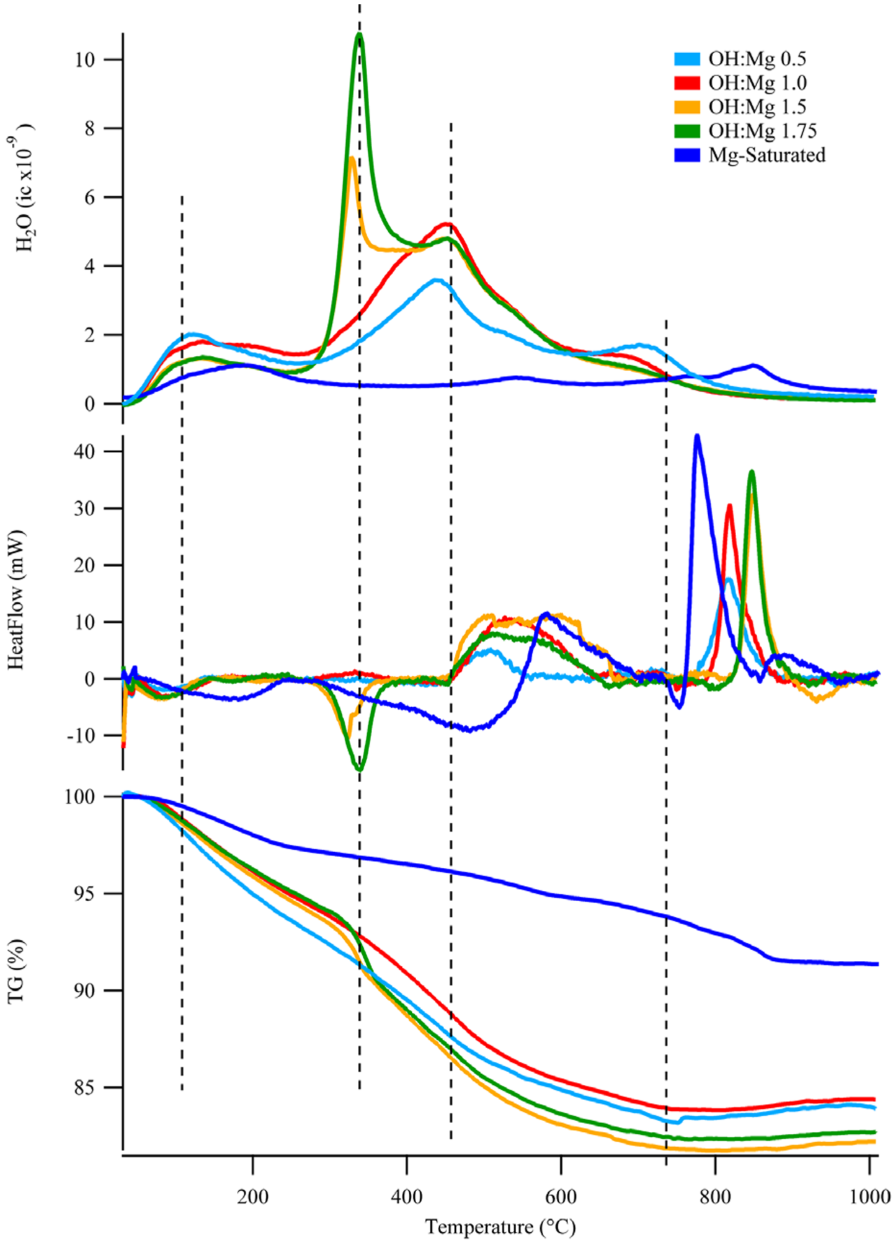

Figure 6. Mass-corrected thermal and evolved gas data for GP saponite samples. Vertical dashed lines are at 105°C, 335°C, 450°C, and 725°C and represent approximate temperatures of major water peaks. Top: EGA traces for m/z=18 (i.e. H_2O). ic = ion current (amps). Middle: baseline-corrected DSC data. Reduced signal of the Mg-saturated sample compared with chloritized samples may be a result of a clog in the mass spectrometer orifice when that sample was analyzed. Bottom: TG data, showing mass loss with increase in temperature.

smectites used in this study. A weak peak at ~3.7 Å is apparent in the OH:Mg=1.75 sample, in particular, which is consistent with the (004) reflection.

Thermal and evolved-gas analysis

GP saponite

All Mg-saturated and chloritized GP saponite samples evolved H_2O (m/z=18) with peaks between 106 and 183°C due to adsorbed and interlayer H_2O, between 439 and 453°C from Fe-OH dehydroxylation in the octahedral sheet, and between 672 and 762°C from Mg-OH dehydroxylation in the octahedral sheet (Fig. 6; see also Table S2 in the Supplementary material; e.g. McAdam et al., 2020). Chloritized samples with OH:Mg ratios of 1.5 and 1.75 evolved additional sharp water releases with peaks at 328°C and 339°C, respectively, from the breakdown of interlayer $Mg(OH)_2$. Low- and mid-temperature water releases co-occurred with DSC endotherms and TG weight losses (Fig. 6A). All Mg-saturated and chloritized GP samples had DSC endotherms immediately followed by exotherms between 755 and 850°C, caused by phyllosilicate dehydroxylation and recrystallization (e.g. Che et al., 2011; McAdam et al., 2020). Water release peaks from 672–710°C decrease in intensity with chloritization, possibly because they are partially obscured by mid-temperature water-release peaks. TG weight loss during pyrolysis generally increased with increasing chloritization. Mg-saturated GP lost 8.6 wt.%, and the chloritized samples lost

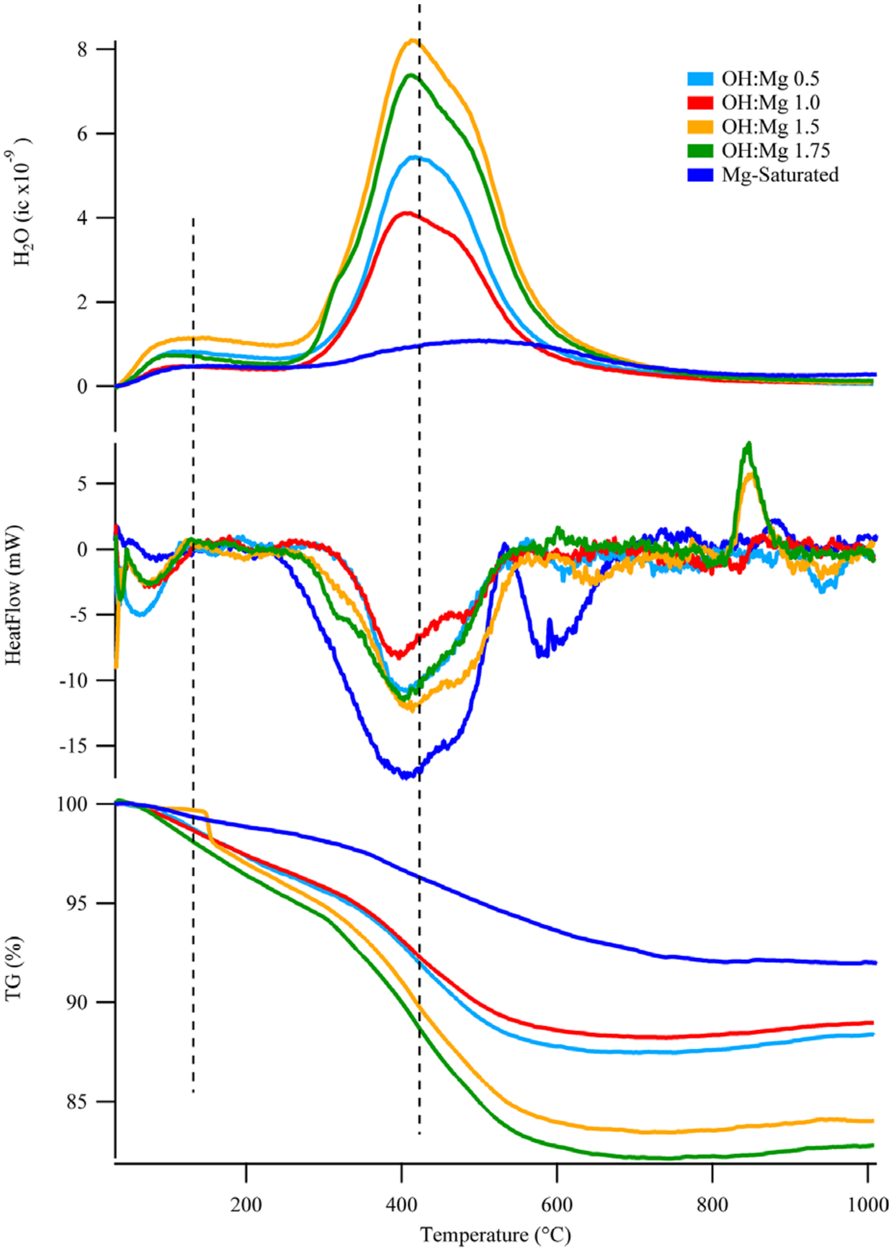

Figure 7. Mass-corrected thermal and evolved gas data for NAu-2 nontronite samples. Vertical dashed lines are at 170°C and 415°C and represent approximate temperatures of major water peaks. Top: EGA traces for m/z=18 (i.e. H_2O). ic = ion current (amps). Reduced signal of the Mg-saturated sample compared with chloritized samples may be a result of a clog in the mass spectrometer orifice when that sample was analyzed. Middle: baseline-corrected DSC data. Bottom: TG data, showing mass loss with increase in temperature.

a total of ~16–18 wt.% (Fig. 6). The greatest difference in TG weight loss between samples occurred over the range 245–725°C.

NAu-2 nontronite

All Mg-saturated and $Mg(OH)_2$ chloritized NAu-2 samples evolved low-temperature adsorbed and interlayer H_2O with peaks between ~85°C and 120°C as well as mid-temperature water releases with peaks between ~405°C and 450°C (Fig. 7; see also Table S2 in the Supplementary material). Mg-saturated and chloritized samples evolved mid-temperature water releases with similar peak temperatures, probably caused by the co-occurrence of dehydroxylation of the nontronite octahedral sheet (~450°C; e.g. Heller-Kallai and Rozenson, 1980; Che et al., 2011; McAdam et al., 2020) and the breakdown of interlayer $Mg(OH)_2$. Low- and mid-temperature water releases co-occurred with DSC endotherms and TG weight losses (Fig. 7). Generally, chloritized samples with greater chloritization (i.e. higher OH:Mg ratios) lost more weight during pyrolysis, and the differences in weight loss occurred over the range ~325–560°C. Total weight loss values from the chloritized NAu-2 nontronite ranged from ~11 to 17 wt.%, whereas Mg-saturated NAu-2 lost ~8 wt.%.

SWy-1 montmorillonite

SWy-1 chloritized samples evolved up to four distinct water-release peaks, whereas Mg-saturated SWy-1 only evolved adsorbed water with a peak at ~110°C and water from the dehydroxylation of the octahedral sheet with a peak at 715°C (Fig. 8; see also Table S2 in the Supplementary material). All chloritized SWy-1 samples evolved

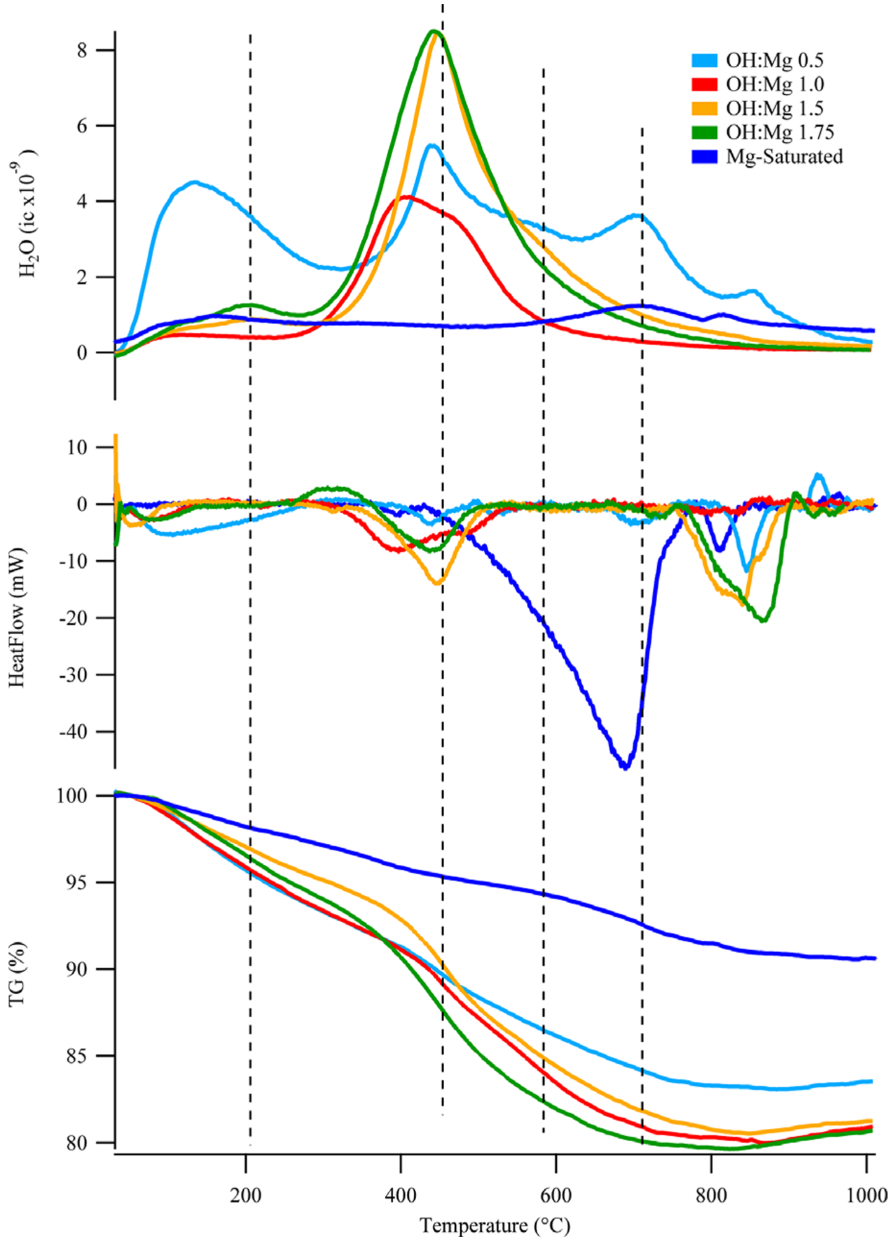

Figure 8. Thermal and evolved gas data for SWy-1 montmorillonite samples. Data are mass-corrected. Vertical dashed lines are at 170°C, 445°C, 575°C, and 715°C and represent approximate temperatures of major water peaks. Top: EGA traces for m/z=18 (i.e. H_2O). ic = ion current (amps). Reduced signal of the Mg-saturated sample compared with chloritized samples may be a result of a clog in the mass spectrometer orifice when that sample was analyzed. Middle: baseline-corrected DSC data. Bottom: TG data, showing mass loss with increase in temperature.

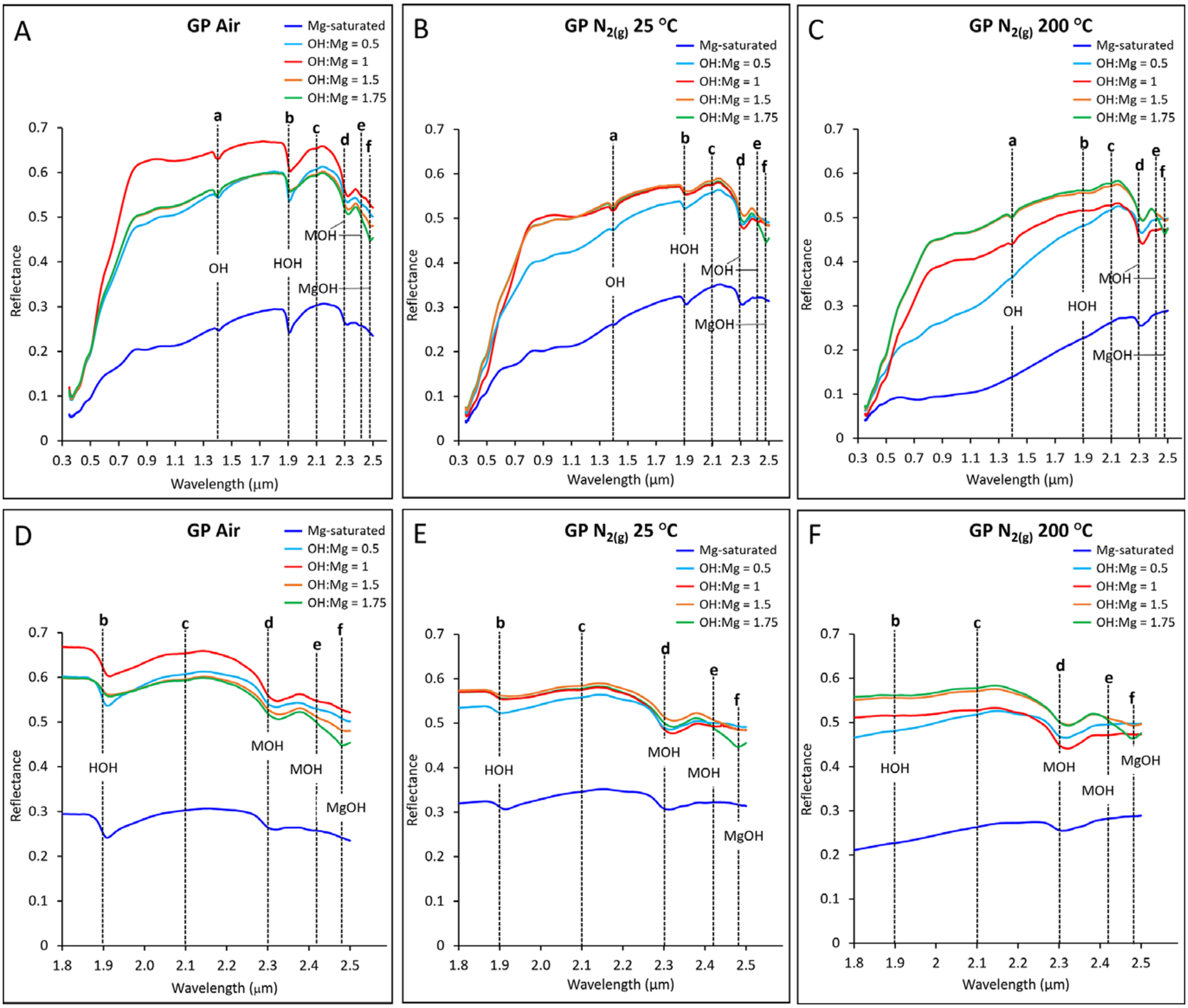

Figure 9. VSWIR reflectance spectra of Mg-saturated and chloritized GP saponite samples. Vertical dashed lines are at 1.40 µm (a), 1.90 µm (b), 2.10 µm (c), 2.30 µm (d), 2.42 µm (e), and 2.48 µm (f). (A,D) VSWIR spectra of GP samples measured under ambient conditions. (B,E) VSWIR reflectance spectra of GP samples measured under dry $N_{2(g)}$ and 25°C. (C,F) VSWIR reflectance spectra of GP samples measured under dry $N_{2(g)}$ and 200°C.

mid-temperature water with peaks between 440°C and ~450°C, and the sample with OH:Mg=0.5 had an additional peak at ~580°C. Mid-temperature water releases are consistent with the breakdown of $Mg(OH)_2$ in the interlayer site. Mg-saturated SWy-1 and the chloritized SWy-1 sample with OH:Mg=0.5 evolved water with peaks between ~705°C and 715°C from dehydroxylation of the montmorillonite octahedral sheet (e.g. Heller-Kallai and Rozenson, 1980; Muller et al., 2000; Che et al., 2011; McAdam et al., 2020). The OH:Mg=0.5 sample also evolved water with a peak at ~855°C. The low- and mid-temperature water releases co-occurred with DSC endotherms. All Mg-saturated and chloritized SWy-1 samples had high-temperature (>700°C) endotherms immediately followed by weak exotherms, which were caused by dehydroxylation of the octahedral sheet and subsequent recrystallization (e.g. Che et al., 2011). Mg-saturated SWy-1 lost a total mass of ~9.4 wt.%, and this value generally increased in samples with higher OH:Mg ratios. The differences in TG mass loss between SWy-1 samples occurred primarily over the temperature range of ~370–670°C, probably related to differences in the extent of chloritization.

VSWIR spectroscopy

GP saponite

VSWIR spectra of Mg-saturated and chloritized GP saponite measured under ambient conditions and at 25°C under $N_{2(g)}$ displayed bands from combinations and overtones of fundamental H_2O stretching and bending modes at 1.39–1.41 µm and 1.91–1.92 µm and from Mg/Fe-OH combination absorptions at ~2.32–2.33 µm, typical of Fe-bearing saponite (Fig. 9; see also Tables S3–S5 in the Supplementary material) (e.g. Clark et al., 1990; Ehlmann et al., 2012; Fox et al., 2021). The ~1.4 µm band was very weak and the ~1.9 µm band was not apparent in samples measured under $N_{2(g)}$ and heated to 200°C because the latter is derived from the fundamental bending vibrations of the H_2O molecule, and H_2O is not present in completely collapsed smectite. Band minima do not shift significantly with sample dehydration. Chloritized samples with OH:Mg=0.5 and 1 had weak bands at ~2.42 µm, and chloritized samples with OH:Mg=1.5 and 1.75 had weak bands at ~2.48 µm, both the result of

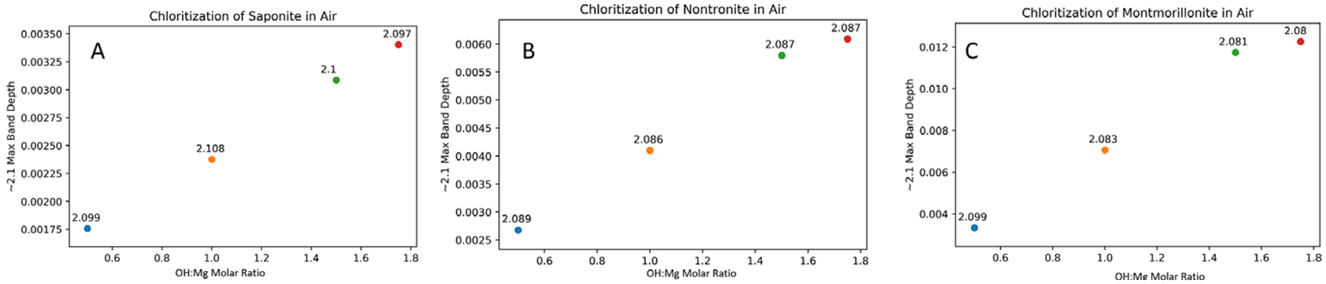

Figure 10. Relationship between the ~2.1 μm band depth and degree of chloritization. (A) ~2.1 μm band depth *versus* OH:Mg molar ratio for GP saponite measured in air. (B) ~2.1 μm band depth *versus* OH:Mg molar ratio for NAu-2 nontronite measured in air. (C) ~2.1 μm band depth *versus* OH:Mg molar ratio for SWy-1 montmorillonite measured in air.

combinations of OH stretching and bending modes. The band at ~2.48 μm appeared as a shoulder in the samples measured under ambient conditions, but became a distinct band when measured under $N_{2(g)}$ at 25°C and 200°C. All spectra of chloritized saponite also had a very weak band at ~2.1 μm that was not apparent in the Mg-saturated spectra. The ~2.1 μm band depth increased with degree of chloritization (i.e. with increase in OH:Mg ratio) (Fig. 10). Weak bands observed at ~2.1 μm in phyllosilicates have been attributed to Mg-OH, Al-OH, and Fe-OH combinations (e.g. Cloutis et al., 2008). The overall low albedo of the Mg-saturated sample relative to the other three samples is attributed to insufficient sample to completely fill the instrument beam diameter on an optically black substrate (see the Methods section).

Very small amounts of Fe and changes in coordination and charge have significant effects on the visible/near-infrared portion of the spectra via electronic absorptions (e.g. Rossman and Ehlmann, 2019). The most prominent characteristic in the visible is an oxygen-metal charge transfer absorption, related to Fe^{3+} and centered in the ultraviolet, therefore creating a reddish edge. This feature shifts to shorter wavelengths with lesser charge, and reduction of some iron during $N_{2(g)}$ purge with heating might drive the diminishment of the red edge. This change was most dramatic in the Mg-saturated sample where the interlayer was most collapsed. The Mg-saturated sample was noticeably darker than those that had undergone chloritization. Speculatively, intervalence charge transfer due to Fe^{2+}–Fe^{3+}, which tends to subdue absorptions over 0.5–1.0 μm (as in magnetite), may be more prevalent in the Mg-saturated sample before further treatment renders samples more ferric. Relatively subtle super-imposed absorptions at ~0.5, 0.65, 0.8, and 0.9 μm were seen in the visible/near-infrared and are consistent with octahedrally coordinated Fe. They do not appear to follow a pattern with treatment and may be due to subtle differences in sample phyllosilicates and nanophase iron oxides, as also seen in subsamples of Griffith saponite (Treiman et al., 2014).

NAu-2 nontronite

The VSWIR spectra of Mg-saturated and chloritized NAu-2 nontronite samples measured under ambient conditions and under $N_{2(g)}$ demonstrate H_2O stretching and bending modes at ~1.4 and at ~1.9 μm and from Mg-OH combination absorptions at ~2.3 μm (Fig. 11; see also Tables S3–S5 in the Supplementary material) are consistent with nontronite spectra (e.g. Clark et al., 1990; Bishop et al., 2002; Ehlmann et al., 2012; Fox et al., 2021). The band at ~1.4 μm is a doublet with minima at 1.39 and 1.43 μm. The ~1.4 μm and ~1.9 μm bands typically weakened with dehydration of samples (i.e. from measurements in air to $N_{2(g)}$ at 25°C to $N_{2(g)}$ at 200°C). Band minima did not shift significantly with sample dehydration. The Mg-saturated and chloritized samples had Mg/Fe-OH combination bands at ~2.3, ~2.4, and ~2.5 μm in all spectra, from combinations of OH stretching and bending modes. All spectra contained very weak bands at ~2.1 μm, which have been observed in phyllosilicates previously and attributed to Mg-OH, Al-OH, and Fe-OH combinations (e.g. Cloutis et al., 2008). The ~2.1 μm band depth increased with degree of chloritization (i.e. with increase in OH:Mg ratio) (Fig. 10). The overall low albedo of the Mg-saturated samples relative to the other three samples is attributed to insufficient sample to completely fill the instrument beam diameter on an optically black substrate (see the Methods section).

Spectra in the visible/near-infrared displayed a prominent red edge from Fe^{3+}-oxygen charge transfer in the UV and super-imposed absorptions from electronic transitions of octahedrally coordinated iron at ~0.5, 0.65, and 0.9 μm. As with the saponite, the samples exhibited a diminished red edge following heating and $N_{2(g)}$ purge.

SWy-1 montmorillonite

The VSWIR spectra of Mg-saturated and chloritized NAu-2 nontronite samples measured under ambient conditions and under $N_{2(g)}$ demonstrate OH and H_2O stretching and bending modes at ~1.4 μm and ~1.9 μm and Mg/Fe(III)/Al-OH combination absorptions at ~2.1 μm to ~2.4 μm (Fig. 12; see also Tables S3–S5 in the Supplementary material), consistent with Mg-bearing montmorillonite (e.g. Clark et al., 1990; Bishop et al., 2002; Ehlmann et al., 2012; Fox et al., 2021). The band minima at ~1.4 μm and ~1.9 μm weakened with dehydration (i.e. from measurements in laboratory air to $N_{2(g)}$ at 25°C to $N_{2(g)}$ at 200°C) in all chloritized and Mg-saturated samples. Samples with OH:Mg=1, 1.5, 1.75 had an additional band at ~2.5 μm when measured under ambient conditions and $N_{2(g)}$ at 25°C. Under $N_{2(g)}$ 200°C, only the chloritized samples with OH:Mg=1.5 and 1.75 had an additional band at ~2.5 μm, which is a combination of OH stretching and bending vibrations.

Spectra in the visible/near-infrared displayed a weak absorption edge possibly from Fe^{3+}–oxygen charge transfer absorption in the UV that is weaker than the other smectites because of a lower Fe concentration (e.g. Mermut and Faz Cano, 2001). Weak electronic transitions at ~0.45, ~0.65, and ~0.9 μm are consistent with the presence of minor Fe^{3+}.

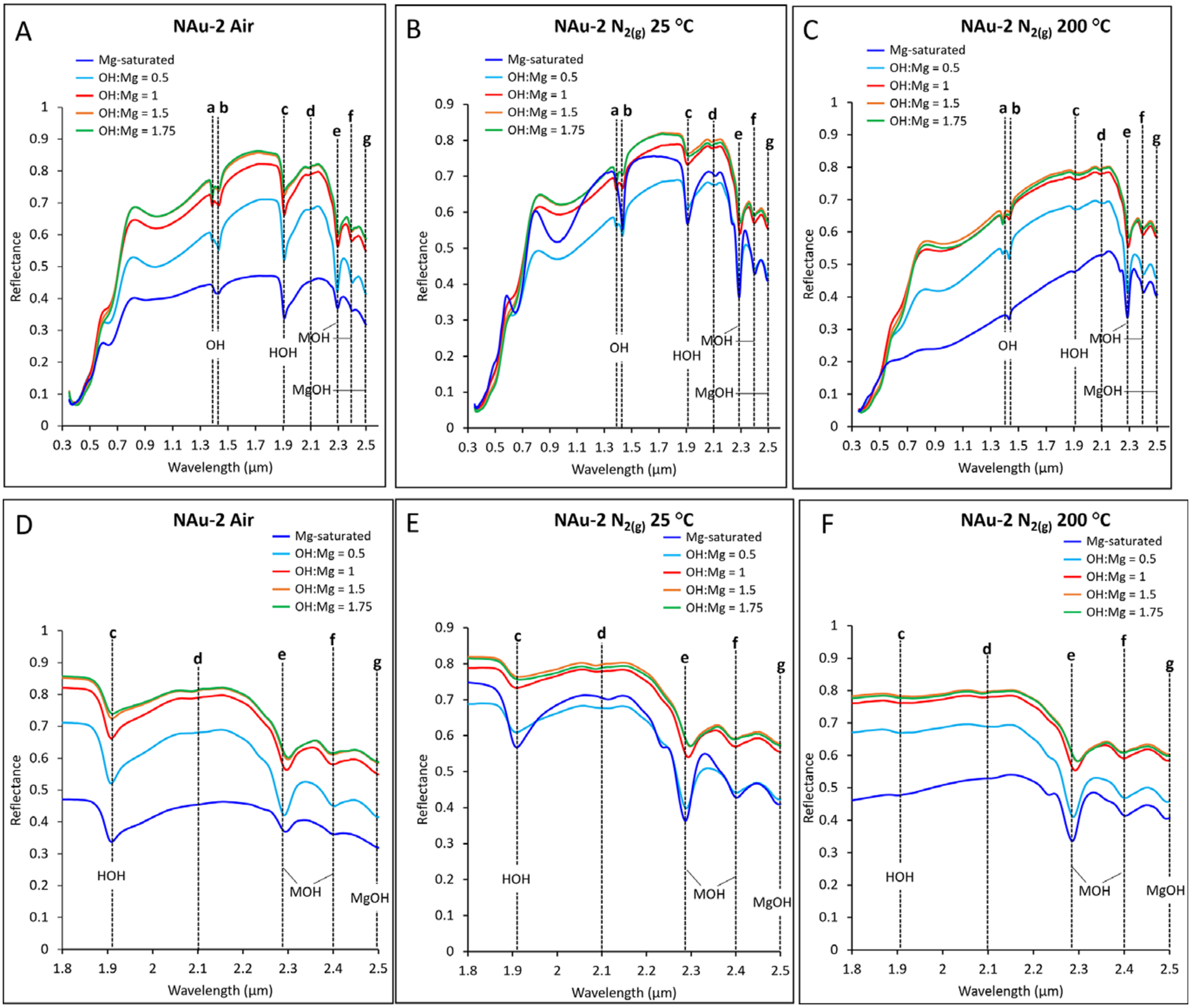

Figure 11. VSWIR reflectance spectra of Mg-saturated and chloritized NAu-2 nontronite. Vertical dashed lines are at 1.39 µm (a), 1.43 µm (b), 1.91 µm (c), 2.10 µm (d), 2.29 µm (e), 2.40 µm (f), and 2.50 µm (g). (A,D) VSWIR spectra of NAu-2 samples measured under ambient conditions. (B,E) VSWIR reflectance spectra of NAu-2 samples measured under dry $N_{2(g)}$ and 25°C. (C,F) VSWIR reflectance spectra of NAu-2 samples measured under dry $N_{2(g)}$ and 200°C.

Discussion

Effects of partial chloritization on XRD, EGA, and VSWIR data

XRD patterns revealed the extent of dehydration and chloritization with changing OH:Mg ratio and the effects of layer charge on chloritization. The heated samples measured under dry $N_{2(g)}$ on the CheMin IV were more dehydrated than the samples measured on the Panalytical under dry $N_{2(g)}$ based on the smaller d_{001} in CheMin IV patterns. At near 0% RH, Mg-saturated smectite is expected to have a d_{001} near 12 Å (e.g. Ferrage et al., 2005), but the Mg-saturated smectite samples measured under dry $N_{2(g)}$ on the Panalytical had d_{001} near 13.5 Å. This discrepancy in peak position suggests that the samples did not fully equilibrate in the dry $N_{2(g)}$ on the Panalytical. Mg-saturated samples measured under $N_{2(g)}$ on the CheMin IV dehydrated more consistently to a d_{001} of <13.5 Å. Thus, patterns for samples that were heated and measured under $N_{2(g)}$ on the CheMin IV best approximate XRD data collected from the very dry surface of Mars.

The XRD patterns demonstrated that treatments successfully produced chloritized smectite samples with increasing OH:Mg ratio. The chloritized smectites measured under dry $N_{2(g)}$ (i.e. with most interlayer water driven off) on the Panalytical and CheMin IV showed an increase in d_{001} from OH:Mg=0.5 to OH:Mg=1.75, indicating the extent of chloritization increased with OH:Mg from more extensive occurrence of brucite-like sheets in the interlayer site. The most dehydrated chloritized smectite samples (i.e. those measured on the CheMin IV under $N_{2(g)}$) showed substantial variability within the same smectite type with different OH:Mg ratios and between smectite types. The ~10 Å d_{001} for Mg-saturated GP saponite indicates that this sample collapsed fully. The 12.9 Å and 13.9 Å d_{001} for Mg-saturated NAu-2 nontronite and SWy-1 montmorillonite, respectively, suggest that these samples were not fully dehydrated before analysis. The increase in d_{001} to 12.2 Å for GP saponite partially chloritized at OH:Mg=0.5 suggests that this sample was partially chloritized, whereas the d_{001} for NAu-2 nontronite and SWy-1 montmorillonite at OH:Mg=0.5 at ~10 Å demonstrates that these samples were not chloritized. This

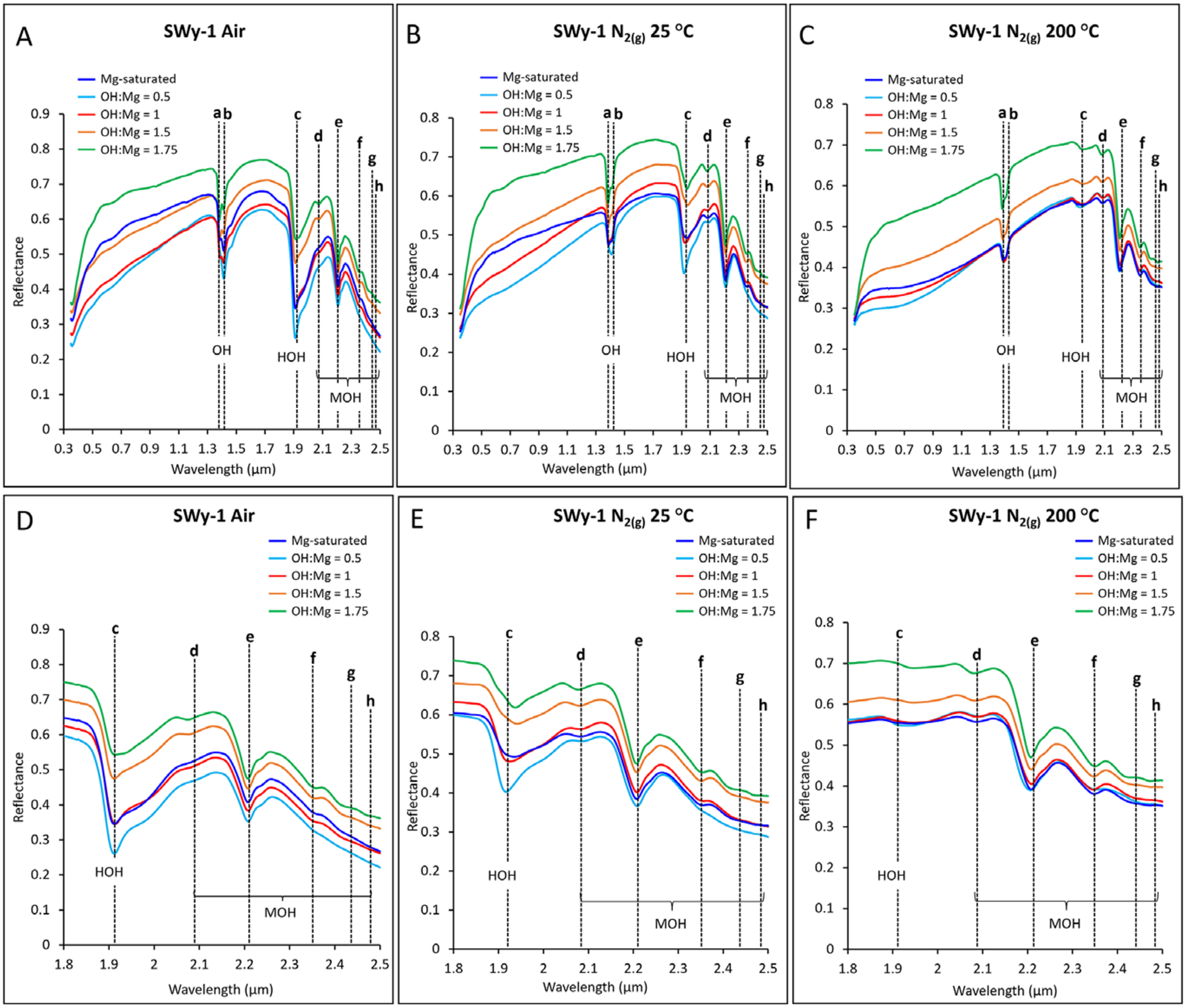

Figure 12. VSWIR reflectance spectra of Mg-saturated and chloritized SWy-1 montmorillonite. Vertical dashed lines are at 1.39 μm (a), 1.41 μm (b), 1.91 μm (c), 2.09 μm (d), 2.21 μm (e), 2.35 μm (f), 2.44 μm (g), and 2.48 μm (h). (A,D) VSWIR spectra of SWy-1 samples measured under ambient conditions. (B,E) VSWIR reflectance spectra of SWy-1 samples measured under dry $N_{2(g)}$ and 25°C. (C,F) VSWIR reflectance spectra of SWy-1 samples measured under dry $N_{2(g)}$ and 200°C.

difference in extent of partial chloritization at the lowest OH:Mg may be related to differences in layer charge between the three smectites. GP saponite is a high-charge smectite (with a total layer charge of –0.74), where most of the layer charge is on the tetrahedral sheet (e.g. Vicente et al., 1996). NAu-2 nontronite has a similar layer charge (–0.7 per unit cell; Gates et al., 2002), where some is tetrahedral (–0.45), and some is octahedral (–0.27). SWy-1 montmorillonite has the lowest layer charge of the three (–0.55), with almost all of the charge associated with the octahedral sheet (e.g. Mermut and Lagaly, 2001). Previous partial chloritization studies on saponite that precipitated gibbsite-like sheets (i.e. Al-OH) in the interlayer site showed that the extent of chloritization is greater for high-charge smectite where the layer charge originates in the tetrahedral sheet (e.g. Kloprogge et al., 1994; Vicente et al., 1997). The high tetrahedral layer charge on the GP saponite may have promoted more complete chloritization at the lowest OH:Mg, resulting in a higher d_{001}. All chloritized smectite samples reached their maximum d_{001} at OH:Mg=1.75 (13.8 Å, 14.3 Å, and 14.4 Å for GP, Nau-2, and Swy-1, respectively).

Based on established methods (e.g. Moore and Reynolds, 1997), NEWMOD software was used to model the basal reflections of the XRD patterns measured on the Panalytical under dry $N_{2(g)}$ and to estimate the extent of chloritization for each sample. The basal reflections were modeled using two phases: (1) discrete collapsed smectite, and (2) mixed-layer chlorite-smectite (C-S). The C-S model provided a valid representation of the experimental products of partial chloritization because the extent to which chlorite interlayer hydroxide sheets are filled can vary. Moreover, the ratio of chlorite-to-smectite is optimized during the modeling procedure, mimicking layer-to-layer differences in susceptibility to chloritization. The hydration state of the smectite layers in C-S was allowed to vary. Model instrument parameters were set to match the experimental set-up (X-ray wavelength = 1.7902 Å, goniometer radius = 24 mm, Søller slit width = 2.3, divergence slit width = 0.5). The degree of chloritization of samples was estimated as the product of the modeled ratio of C-S to discrete smectite, the percentage C content of C-S, and the occupancy of the chlorite interlayer hydroxide sites. For example, the measured XRD pattern of the GP saponite with OH:Mg=0.5 was

Table 2. Estimated degree of chloritization of laboratory-chloritized smectites and the CheMin Cumberland sample.

Sample ID	Percent C-S	Percent C in C-S	Percent chlorite interlayer hydroxide occupancy	Estimated degree of chloritization
GP OH:Mg 0.5	77	80	69	43
GP OH:Mg 1.0	74	85	100	63
GP OH:Mg 1.5	81	95	100	77
GP OH:Mg 1.75	84	94	100	79
NAu-2 OH:Mg 0.5	Not modeled*			
NAu-2 OH:Mg 1.0	80	77	89	55
NAu-2 OH:Mg 1.5	94	70	100	66
NAu-2 OH:Mg 1.75	100	73	100	73
Swy-1 OH:Mg 0.5	92	62	67	38
Swy-1 OH:Mg 1.0	93	65	90	54
Swy-1 OH:Mg 1.5	94	72	98	66
Swy-1 OH:Mg 1.75	96	88	100	84
Cumberland	93	70	92	60

Estimates were derived from NEWMOD models of measured XRD patterns. *The NAu-2 OH:Mg 0.5 XRD pattern was too complex to model using the approach outlined in the main text because of the presence of smectite in various hydration states.

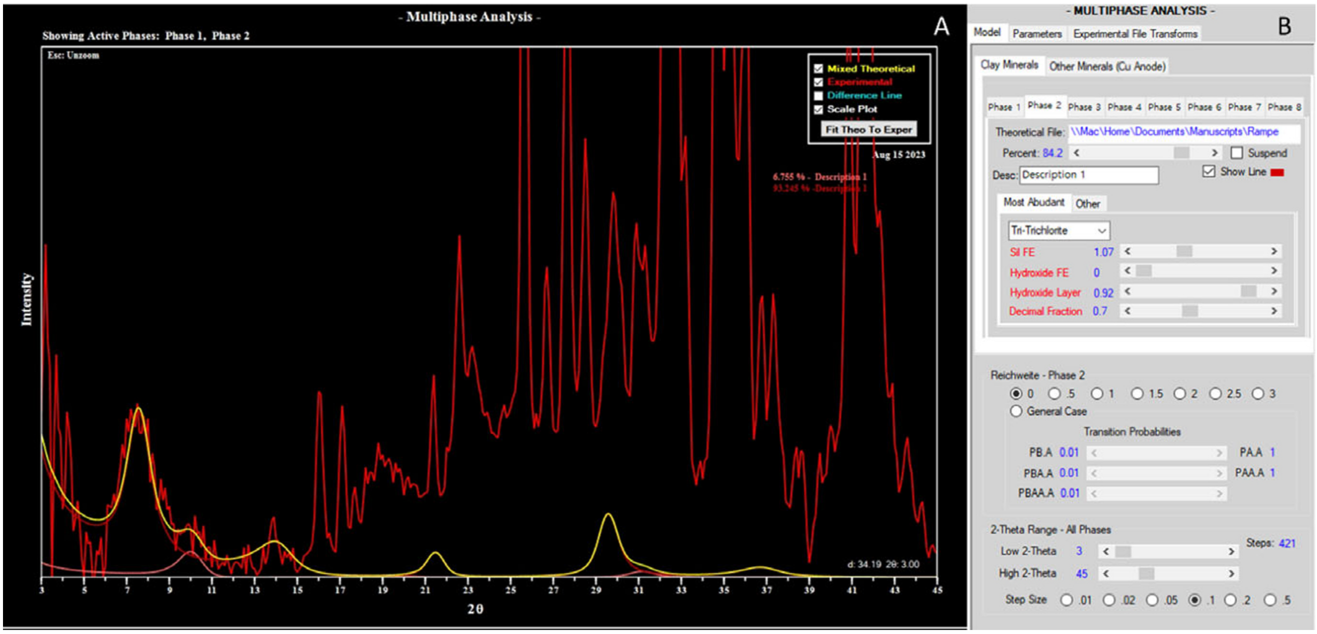

Theoretical File: \\Mac\Home\Documents\Manuscripts\Rampe
Percent: 84.2 ☐ Suspend
Desc: Description 1 ☑ Show Line
Tri-Trichlorte
Sil FE 1.07
Hydroxide FE 0
Hydroxide Layer 0.92
Decimal Fraction 0.7
Reichweite - Phase 2
● 0 ○ .5 ○ 1 ○ 1.5 ○ 2 ○ 2.5 ○ 3
○ General Case
Transition Probabilities
PB.A 0.01 PA.A 1
PBA.A 0.01 PAA.A 1
PBAA.A 0.01
2-Theta Range - All Phases
Low 2-Theta 3
High 2-Theta 45
Steps: 421
Step Size ○ .01 ○ .02 ○ .05 ● .1 ○ .2 ○ .5

Figure 13. Model of degree of chloritization in Cumberland. (A) NEWMOD model (yellow trace) of the basal phyllosilicate reflections in the Cumberland CheMin XRD pattern (red pattern). The yellow trace is a linear combination of a mixed-layer chlorite-smectite (red trace) and a discrete collapsed smectite (pink trace). The model uses ~93 wt.% chlorite-smectite and ~7 wt.% discrete collapsed smectite. (B) Graphical user interface of NEWMOD showing relevant modeled parameters. Hydroxide layer refers to the occupancy of the hydroxide interlayer sheets of the chlorite layers in C-S (92% in this model). Decimal fraction refers to the weight per cent chlorite in the C-S (70% in this model).

best fit by a model containing a mixture of 77% C-S and 23% discrete collapsed smectite, with C-S containing 80% chlorite layers, and a chlorite interlayer hydroxide site occupancy of 69%. Thus, resulting in an estimated degree of chloritization of 77%×80%×69%=43% (Table 2; see also Figs S4–S14 in the Supplementary material). NEWMOD-derived estimates of the degree of chloritization of smectite standards all increase with increasing OH:Mg in the chloritizing solutions.

NEWMOD was also used to model the basal phyllosilicate reflections of the Cumberland CheMin XRD pattern, using a similar approach. NEWMOD's background correction function was applied (Fig. 13) to the Cumberland pattern to account for amorphous material contributions – the 'low-angle rise' commonly observed in amorphous-bearing samples (e.g. Pandey et al., 2023) – that may influence the apparent position of basal reflections. Modeling suggests that the phyllosilicate in this drill target is

~93% mixed-layer chlorite-ferrian saponite and ~7% collapsed ferrian saponite (Fig. 13). The modeled percentage C content of C-S is ~70%, with ~92% of the hydroxide interlayer sites of the chlorite filled by $Mg(OH)_2$. The calculations from these model results suggest that the smectite in Cumberland is ~60% chloritized, similar to smectites exposed to fluids with OH: Mg=1.0 in the laboratory syntheses presented here. This finding indicates that there was insufficient Mg^{2+} or OH^- in solution to fully chloritize the smectite in Cumberland, suggesting further that the interaction between saponite in Yellowknife Bay and alkaline Mg^{2+}-bearing fluids was relatively brief.

EGA data demonstrated that partial chloritization with Mg(OH) results in a distinct H_2O release peak near 450°C that may be a defining characteristic of this type of partial chloritization. This peak was apparent in all chloritized samples and increased in intensity with higher OH:Mg ratios (i.e. with greater extent of chloritization), demonstrating that more Mg–OH bonds are broken with pyrolysis. GP saponite samples with the highest OH: Mg (i.e. 1.5 and 1.75) had an additional sharp peak at 335°C, which is consistent with the thermal decomposition of brucite (e.g. Gallagher, 1982). The H_2O release from the breakdown of Mg-OH bonds in the interlayer site of chloritized NAu-2 nontronite samples overlapped the H_2O release from the breakdown of Fe(III)-OH bonds in the octahedral site. This overlap indicates EGA cannot be used to definitively identify nontronite chloritized with brucite-like sheets.

Chloritization appears to destabilize the structure of the GP saponite and SWy-1 montmorillonite octahedral sheets somewhat. The Mg-saturated GP saponite EGA data showed an H_2O release at ~850°C from the dehydroxylation of the Mg–OH bonds in the octahedral sheet (e.g. McAdam et al., 2020). With increasing degree of chloritization, this release shifted to lower temperatures (~700°C) and became weaker, suggesting that the octahedral sheet is less stable than in the parent saponite and that fewer Mg-OH bonds are available to break. EGA data from SWy-1 montmorillonite showed that the peak at ~715°C from the dehydroxylation of the Al-OH bonds in the octahedral sheet either disappears with increasing degree of partial chloritization or shifts to lower temperatures (~575°C) to account for an asymmetric release at 445°C. The disruption of the octahedral sheet was not observed by XRD (i.e. the (06*l*) peak positions and intensities did not vary), so this disruption is probably not substantial. Alternatively, partial chloritization with Mg-OH may catalyze the dehydroxylation of saponite and montmorillonite octahedral sheets, where the release of H_2O at ~425°C from the breakdown of interlayer brucite-like sheets destabilizes the mineral structure and allows the breakdown of octahedral sheets at lower temperatures. This catalysis does not happen in nontronite because the dehydroxylation of the brucite-like sheets and the Fe–OH bonds in the octahedral sheet occur at the same temperature.

Partial chloritization of GP saponite, NAu-2 nontronite, and SWy-1 saponite had an effect on VSWIR reflectance spectra but did not produce strong diagnostic bands that could be identified easily on the Martian surface from orbit or *in situ*. The primary vibrational bands used to identify phyllosilicates in the laboratory and on Mars (i.e. M-OH overtones between ~2.2 and ~2.3 μm) were not affected by partial chloritization, further suggesting that the structure of the parent smectite is not substantially changed by partial chloritization. VSWIR laboratory measurements in air and under dry $N_{2(g)}$ at 25°C typically exhibited decreased ~1.9 μm H_2O band intensity with an increase in partial chloritization from the replacement of interlayer H_2O with interlayer brucite-like sheets. The GP saponite samples chloritized with OH:Mg=1.5 and 1.75 had

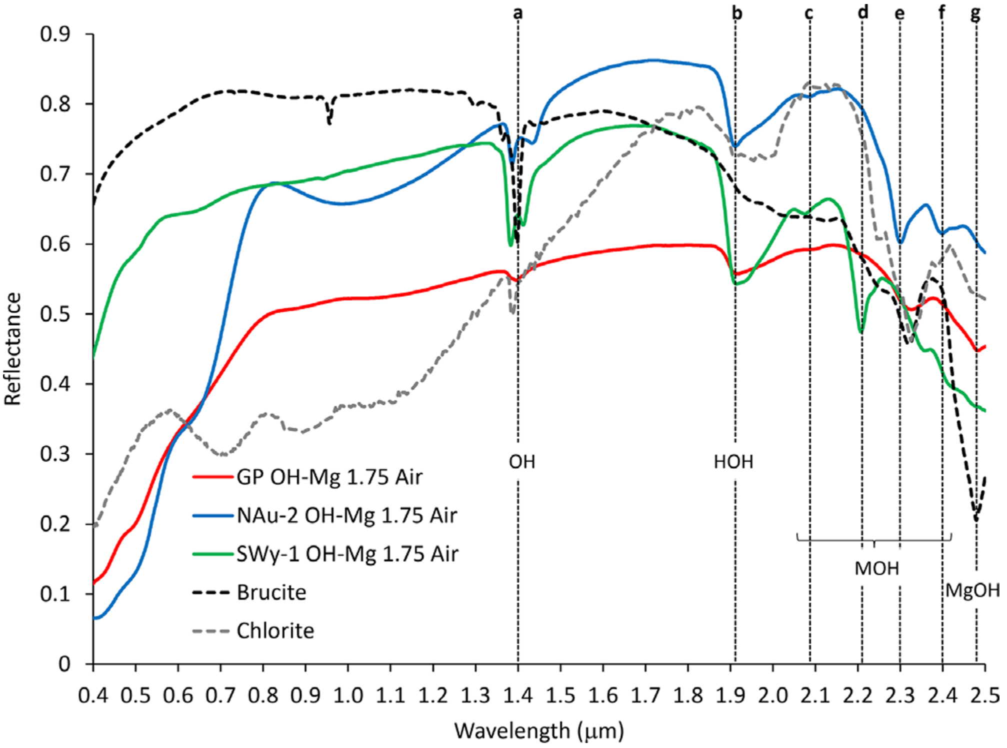

Figure 14. Comparisons of VSWIR reflectance spectra of partially chloritized smectite, Mg-rich chlorite, and brucite. VSWIR reflectance spectra of OH:Mg=1.75 partially chloritized GP saponite (red), NAu-2 nontronite (blue), and SWy-1 montmorillonite (green) measured in air and brucite (black dashed) and Mg-rich chlorite (gray dashed). Brucite and Mg-rich chlorite spectra are from the USGS Spectral Library (Brucite_HS247.1B_ASDFRc_AREF and Chlorite_SMR-13.d_30-45um_BECKa_AREF, respectively) (Kokaly et al., 2017). Vertical dashed lines are at 1.4 μm (a), 1.91 μm (b), 2.09 μm (c), 2.21 μm (d), 2.3 μm (e), 2.4 μm (f), and 2.48 μm (g) for reference.

Table 3. Comparisons of XRD and EGA observations in Cumberland (CB), John Klein (JK), partially chloritized GP saponite, and Mg-saturated GP saponite.

	CB observations	JK observations	GP OH:Mg 1.0	GP Mg-sat
XRD*	Peaks at 13.5, 7.4, and 4.59 Å	Peak at 4.59 Å, shoulder at *d* spacing >10 Å	Peaks at 13.6, 7.4, and 4.59 Å	Peaks at 9.9 and 4.60 Å
EGA	Water releases at 453°C and 725°C	Water releases at 462°C and 725°C	Water releases at 453°C and 662°C	Water releases at 535°C and 764°C

*Laboratory XRD observations are from measurements in the CheMin IV under dry $N_{2(g)}$ after heating.

a weak band at 2.48 µm, which was also seen in spectra of brucite (e.g. Beck et al., 2015) and, therefore, is not a unique characteristic of Mg-OH partial chloritization (Fig. 14).

The weak band at ~2.1 µm may be a marker of degree of partial chloritization; the intensity of the 2.1 µm band increased with increasing degree of chloritization (Fig. 10). This band was previously recognized in laboratory spectra of a variety of smectite samples and was assigned to Mg-OH, Al-OH, and Fe-OH combinations (e.g. Cloutis et al., 2008). A weak band at ~2.1 µm is also present in brucite (e.g. Beck et al., 2015), and thus it is not uniquely attributable to chloritization of smectite (Fig. 14). Additional complications with using this peak to identify chloritized smectite on Mars is that this band is probably too weak to be identified in CRISM data above the noise threshold and is in the same location as some sulfate bands (e.g. Cloutis et al., 2008). The ~2.1 µm band may be useful when used in concert with other datasets on landed missions. For example, VSWIR reflectance spectra from SuperCam on the Mars2020 *Perseverance* rover (Wiens et al., 2021) with a signature of smectite with a weak ~2.1 µm band, combined with spatial geochemical data from the Planetary Instrument for X-ray Lithochemistry (PIXL) (Allwood et al., 2020) that showed an enrichment in Mg, would be consistent with Mg-OH chloritized smectite, but detailed structural analyses on the clay minerals in returned samples would be necessary to confirm this hypothesis.

Evidence for partial chloritization in Gale crater and implications for aqueous environments

CheMin XRD and SAM EGA data are consistent with the presence of partially chloritized saponite at the base of the stratigraphic section in Yellowknife Bay (Table 3). The CheMin XRD pattern of the Cumberland drill powder shows a (001) peak at ~13.5 Å and a shoulder at 10 Å, and the XRD pattern of the John Klein powder shows a (001) peak at 10 Å with a shoulder at higher *d*-spacings (Fig. 1; Vaniman et al., 2014). The (02*l*) peaks of these drill powders and the H_2O release at 725°C from SAM data demonstrate that the clay mineral present is Fe^{3+}-bearing saponite (Ming et al., 2014; Treiman et al., 2014; Vaniman et al., 2014; Bristow et al., 2015). Measurements of chloritized smectite under dry $N_{2(g)}$ showed that partial chloritization with Mg-OH can produce expanded (001) peaks under Martian conditions, like those seen in Cumberland and John Klein patterns. It was previously proposed that an interlayer cation with a high hydration energy (e.g. Mg^{2+}) could also cause an expanded smectite structure in Cumberland and John Klein (Ming et al., 2014; Vaniman et al., 2014; Bristow et al., 2015; Fukushi et al., 2019). However, the observation here of complete collapse of heat-desiccated Mg-saturated GP saponite measured under $N_{2(g)}$ on the CheMin IV indicates that partial chloritization of saponite is necessary to explain the expanded structures in Cumberland and John Klein. Cumberland has a weak diffraction peak at ~7.4 Å,

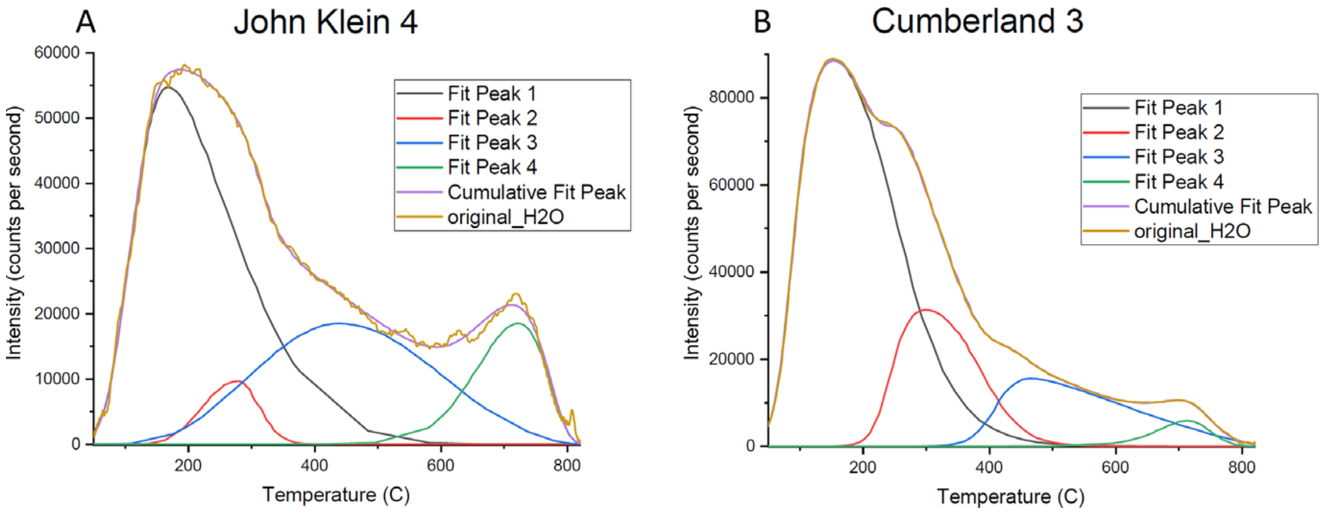

Figure 15. Fitting SAM H_2O EGA traces from John Klein (A) and Cumberland (B). Yellow traces show the original SAM data and purple curves are the cumulative fits from the four individual H_2O peaks identified in the models. SAM data from John Klein and Cumberland show shoulders near 450°C that are modeled with peaks shown as blue curves.

Table 4. H_2O associated with the ~450°C peak in SAM data from John Klein (JK) and Cumberland (CB)

	Peak *T*	Per cent H_2O in ~450°C peak	Uncert.	Moles H_2O in ~450°C peak	Uncert.	Total wt.% H_2O in sample	Uncert.	Wt.% H_2O in ~450°C peak	Uncert.
JK4	453	24.6	0.6	1.10×10^{-5}	1.33×10^{-6}	1.79	1.16	0.44	0.28
CB3	462	11.1	0.9	6.92×10^{-6}	5.57×10^{-7}	2.49	1.61	0.29	0.18

which was previously attributed to the (101) peak in akaganeite (Vaniman et al., 2014). This peak may be the (002) peak of partially chloritized smectite in this mudstone.

SAM H_2O release data are also consistent with the presence of Mg-OH partially chloritized saponite in Cumberland and John Klein. Fitting peaks in the SAM H_2O release data revealed a shoulder near 450°C, which is in the temperature range of interlayer Mg-OH dehydroxylation (Fig. 15). Although nontronite also dehydroxylates at this temperature (Fig. 7), the lack of a (02*l*) peak diagnostic of a dioctahedral smectite in CheMin data of John Klein and Cumberland indicates that nontronite cannot explain the EGA 450°C peaks from both drill samples. Models of SAM H_2O EGA traces showed that ~25% of the total water in John Klein is accounted for by this peak, whereas ~11% of the total water in Cumberland is accounted for by this peak (Table 4). This discrepancy is the result of greater relative amounts of low-temperature water in Cumberland compared with John Klein, which could be associated with interlayer H_2O in the smectite structure or H_2O adsorbed to X-ray amorphous materials (Ming et al., 2014).

The presence of saponite partially chloritized with $Mg(OH)_2$ in Yellowknife Bay is consistent with limited interaction with alkaline Mg-bearing fluids. Raised ridges enriched in Mg observed in the bedrock that hosts the Cumberland and John Klein drill holes suggest these Mg-rich alkaline fluids were present during early diagenesis before the sediments lithified (Léveillé et al., 2014). Chloritized smectite is also consistent with thermochemical models that show alteration of Fe-rich basalt in CO_2-poor and oxidizing solutions with a pH of ~7.5–12 and can explain the secondary mineral assemblage in Yellowknife Bay (Bridges et al., 2015). Such alkaline Mg^{2+}-bearing fluids would be expected for fluids buffered by the basaltic sediments observed in Yellowknife Bay (e.g. Tosca and McLennan, 2006). Chloritization of saponite by Mg^{2+}-rich alkaline pore waters has been observed in rocks and sediments on Earth. Evaporative, alkaline environments can produce chloritic material with incomplete layer sheets (e.g. Weaver, 1989; Bristow and Milliken, 2011). Jurassic-aged lake sediments from the East Berlin formation of the Connecticut Valley contain chloritized smectite but lack salts typical of an alkaline lake evaporation sequence, suggesting chloritization happened during early diagenesis, rather than as a result of evaporation of lake waters at the surface (April, 1981). A lack of abundant salts or morphological features indicative of desiccation at Yellowknife Bay (e.g. McLennan et al., 2014; Vaniman et al., 2014) suggests similarly that partial chloritization occurred during early diagenesis rather than during evaporation of the lake waters.

Smectite is observed throughout most of the 600+ m stratigraphic section studied by *Curiosity* so far, but Yellowknife Bay is the only location where an expanded structure is observed (e.g. Rampe et al., 2020a; Tu et al., 2021; Thorpe et al., 2022). The limited extent of partially chloritized smectite in Gale crater suggests that alkaline Mg^{2+}-bearing fluids did not commonly interact with smectite-bearing units. The location of Yellowknife Bay within Gale crater may explain why this mudstone is the only outcrop that shows evidence for partially chloritized smectite across *Curiosity*'s traverse. Yellowknife Bay is at the base of the stratigraphic section, making it a natural place for diagenetic fluids to collect. As the fluids interacted with the buried lake sediments in a closed system, the pH would be buffered by basaltic primary minerals, releasing basic cations, including Mg^{2+}, and creating alkaline fluids. Open-system alteration at higher elevations investigated by *Curiosity* (i.e. on the lower slopes of Mount Sharp) would preclude formation of alkaline fluids because of a shorter residence time. Indeed, observation of a change from trioctahedral to dioctahedral smectite going up section indicates a transition from closed- to open-system alteration (Bristow et al., 2018).

Putting the results from Yellowknife Bay in context with the mineralogy of the rest of the stratigraphic section demonstrates a diversity of diagenetic conditions in Gale crater. The observation of variable amounts of akaganeite, jarosite, red and gray hematite, magnetite, and carbonate suggests diagenetic fluids varied in pH, salinity, redox conditions, and temperature (e.g. Rampe et al., 2017; Rampe et al., 2020a; Rampe et al., 2020b; Bristow et al., 2021; Thorpe et al., 2022). The recent orbital and *in situ* detections of hydrated Mg-sulfate salts in units above the smectite-bearing strata (e.g. Sheppard et al., 2020; Chipera et al., 2023) and the detection of siderite ($FeCO_3$) *in situ* (e.g. Morrison et al., 2024) suggests that saline Mg^{2+}- and HCO_3^--bearing fluids may have been more common later in Gale crater's history. The absence of smectite in these rocks, however, precluded partial chloritization reactions.

Supplementary material. To view supplementary material for this article, please visit http://doi.org/10.1017/cmn.2024.42.

Data availability statement. Laboratory data presented in this manuscript are available in the supplementary material. Data from CheMin and SAM are available in the Planetary Data System (https://pds-geosciences.wustl.edu/msl/). CheMin data are also available in the Open Data Repository (http://odr.io/CheMin).

Acknowledgements. The authors thank Michael Thorpe for the use of the NEWMOD software, and Brad Sutter for his thoughtful comments on the manuscript.

Author contribution. EBR conceived the project, designed the chloritization experiments, made laboratory measurements, interpreted laboratory and CheMin data, and wrote the manuscript. VMT helped design the chloritization experiments, made laboratory XRD measurements, interpreted laboratory XRD and VSWIR data, and helped write the manuscript. RVM collected, processed, and interpreted laboratory VSWIR data and edited the manuscript.JVC collected and interpreted laboratory EGA data and helped write and edit the manuscript.TFB interpreted laboratory XRD data, performed NEWMOD analyses, and helped write and edit the manuscript. BLE interpreted laboratory VSWIR data and helped write and edit the manuscript. SP performed chloritization experiments and collected XRD data. VC performed chloritization experiments and collected XRD data. BR interpreted laboratory VSWIR data. DWM helped conceive of the project and edited the manuscript. PDA helped conceive of the project and edited the manuscript.

Financial support. This work was funded by the NASA Solar System Workings Program, grant #80NSSC18K1535, and by the ISFM Mission Enabling Science Work Package at the Johnson Space Center.

Competing interest. The authors declare none.

References

Allwood, A.C., Wade, L.A., Foote, M.C., Elam, W.T., Hurowitz, J.A., Battel, S., & 91 co-authors (2020). PIXL: Planetary Instrument for X-ray Lithochemistry. *Space Science Reviews*, *216*, 134. https://doi.org/10.1007/s11214-020-00767-7

April, R.H. (1981). Trioctahedral smectite and interstratified chlorite/smectite in Jurassic strata of the Connecticut Valley. *Clays and Clay Minerals*, *29*, 31–39.

Barnhisel, R. I., & Bertsch, P. L. (1989). Chlorites and hydroxy-interlayered vermiculite and smectite. In *Minerals in Soil Environments*, ed. Dixon, J.B., & Weed, S.B., pp. 729–788. Soil Science Society of America, Madison, WI, USA.

Beck, P., Schmidt, B., Cloutis, E.A., & Vernazza, P. (2015). Low-temperature reflectance spectra of brucite and the primitive surface of 1-Ceres? *Icarus*, *257*, 471–476. https://doi.org/10.1016/j.icarus.2015.05.031

Bishop, J. L., Murad, E., & Dyar, M.D. (2002). The influence of octahedral and tetrahedral cation substitution on the structure of smectites and serpentines as observed through infrared spectroscopy. *Clay Minerals*, *37*, 617–628.

Blake, D., Vaniman, D., Achilles, C., Anderson, R., Bish, D., Bristow, T., Chen, C., Chipera, S., Crisp, J., Des Marais, D., Downs, R.T., Farmer, J., Feldman, S., Fonda, M., Gailhanou, M., Ma, H., Ming, D.W., Morris, R.V., Sarrazin, P., Stolper, E., Treiman, A., & Yen, A. (2012). Characterization and calibration of the CheMin mineralogical instrument on Mars Science Laboratory. *Space Science Reviews*, *170*, 341–399. https://doi.org/10.1007/s11214-012-9905-1

Bridges, J.C., Schwenzer, S.P., Leveille, R., Westall, F., Wiens, R.C., Mangold, N., Bristow, T., Edwards, P., & Berger, G. (2015). Diagenesis and clay mineral formation at Gale crater, Mars. *Journal of Geophysical Research: Planets*, *120*, 1–19. https://doi.org/10.1002/2014JE004757

Brindley, G.W. (1952). Identification of clay minerals by X-ray diffraction analysis. *Clays and Clay Minerals*, *1*, 119–129.

Bristow, T.F., & Milliken, R.E. (2011). Terrestrial perspective on authigenic clay mineral production in ancient Martian lakes. *Clays and Clay Minerals*, *59*, 339–358.

Bristow, T.F., Bish, D.L., Vaniman, D.T., Morris, R.V., Blake, D.F., Grotzinger, J. P., Rampe, E.B., Crisp, J.A., Achilles, C.N., Ming, D.W., Ehlmann, B.L., King, P.L., Bridges, J.C., Eigenbrode, J.L., Sumner, D.Y., Chipera, S.J., Moorokian, J. M., Treiman, A.H., Morrison, S.M., Downs, R.T., Farmer, J.D., Des Marais, D., Sarrazin, P., Floyd, M.M., Mischna, M.A., & McAdam, A.C. (2015) The origin and implications of clay minerals from Yellowknife Bay, Gale crater, Mars. *American Mineralogist*, *100*, 824–836.

Bristow, T.F., Rampe, E.B., Achilles, C.N., Blake, D.F., Chipera, S.J., Craig, P., Crisp, J.A., Des Marais, D.J., Downs, R.T., Gellert, R., Grotzinger, J.P., Gupta, S., Hazen, R.M., Horgan, B., Hogancamp, J.V., Mangold, N., Mahaffy, P.R., McAdam, A.C., Ming, D.W., Morookian, J.M., Morris, R.V., Morrison, S.M., Treiman, A.H., Vaniman, D.T., Vasavada, A.R. & Yen, A.S. (2018). Clay mineral diversity and abundance in sedimentary rocks of Gale crater, Mars. *Science Advances* (6), eaar3330.

Bristow, T.F, Grotzinger, J.P., Rampe, E.B., Cuadros, J., Chipera, S.J., Downs, G., Fedo, C.M., Frydenvang, J., McAdam, A.C, Achilles, C.N., Blake, D.F., Castle, N., Craig, P.I., Des Marais, D.J., Downs, R.T., Hazen, R.M., Ming, D.W., Morris, R.V., Morrison, S.M., Thorpe, M.T., Treiman, A.H., Tu, V., Vaniman, D.T., Yen, A.S., Gellert, R., Mahaffy, P.R., Wiens, R.C., Bryk, A.B., Bennett, K. A., Fox, V.K., Milliken, R.E., Fraeman, A.A., & Vasavada, A.R. (2021). Brine driven diagenesis of clay minerals in Gale crater, Mars. *Science*, *373*, 198–204.

Cannon, K.M., Parman, S.W., & Mustard, J.F. (2017). Primordial clays on Mars formed beneath a steam or supercritical atmosphere. *Nature*, *552*, 88–91.

Che, C., Glotch, T.D., Bish, D.L., Michalski, J.R., & Xu, W. (2011). Spectroscopic study of the dehydration and/or dehydroxylation of phyllosilicate and zeolite minerals. *Journal of Geophysical Research: Planets*, *116*, E5. https://doi.org/10.1029/2010JE003740

Chipera, S.J., Vaniman, D.T., Rampe, E.B., Bristow, T.F., Martínez, G., Tu, V.M., Peretyazhko, T.S., Yen, A.S., Gellert, R., Berger, J.A., Rapin, W., Morris, R.V., Ming, D.W., Thompson, L.M., Simpson, S., Achilles, C.N., Tutolo, B., Downs, R.T., Fraeman, A.A., Fischer, E., Blake, D.F., Treiman, A.H., Morrison, S.M., Thorpe, M.T., Downs, G., Castle, N., Craig, P.I., Des Marais, D.J., Hazen, R. M., Vasavada, A.R., Hausrath, E., Sarrazin, P., & Grotzinger, J.P. (2023). Mineralogical investigation of Mg-sulfate at the Canaima drill site, Gale crater, Mars. *Journal of Geophysical Research: Planets*, *128*. https://doi.org/10.1029/2023JE008041

Clark, R. N., King, T. V. V., Klewja, M., Swayze, G.A., & Vergo, N. (1990). High resolution reflectance spectroscopy of minerals. *Journal of Geophysical Research*, *95*, 12653–12680. https://doi.org/10.1029/JB095iB08p12653

Cloutis, E.A., Craig, M.A., Kruzelecky, R.V., Jamroz, W.R., Scott, A., Hawthorne, F.C., & Mertzman, S.A. (2008). Spectral reflectance properties of minerals exposed to simulated Mars surface conditions. *Icarus*, *195*, 140–168. https://doi.org/10.1016/j.icarus.2007.10.028

Ehlmann, B.L., Mustard, J.F., Murchie, S.L., Bibring, J.-P., Meunier, A., Fraeman, A.A., & Langevin, Y. (2011). Subsurface water and clay mineral formation during the early history of Mars. *Nature*, *479*, 53–60.

Ehlmann, B. L., Bish, D.L., Ruff, S.W., & Mustard, J.F. (2012). Mineralogy and chemistry of altered Icelandic basalts: application to clay mineral detection and understanding aqueous environments on Mars. *Journal of Geophysical Research*, *117*. https://doi.org/10.1029/2012JE004156

Ehlmann, B.L., Berger, G., Mangold, N., Michalski, J.R., Catling, D.C., Ruff, S.W., Chassefière, E., Niles, P.B., Chevrier, V., & Poulet, F. (2013). Geochemical consequences of widespread clay mineral formation in Mars' ancient crust. *Space Science Reviews*, *174*, 329–364. https://doi.org/10.1007/s11214-012-9930-0

Ferrage, E., Lanson, B., Sakharov, B.A., & Drits, V.A. (2005). Investigation of smectite hydration properties by modeling experimental X-ray diffraction patterns. *Part I. Montmorillonite hydration properties.* American Mineralogist, *90*, 1358–1374.

Fox, V.K., Kupper, R.J., Ehlmann, B.L., Catalano, J.G., Razzell-Hollis, J., Abbey, W.J., Schild, D.J., Nickerson, R.D., Peters, J.C., Katz, S.M., & White, A.C. (2021). Synthesis and characterization of Fe(III)-Fe(II)-Mg-Al smectite solid solutions and implications for planetary science. *American Mineralogist*, *106*. https://doi.org/10.2138/am-2020-7419CCBYNCND.

Fukushi, K., Sekine, Y., Sakuma, H., Morida, K., & Wordsworth, R. (2019). Semiarid climate and hyposaline lake on early Mars inferred from reconstructed water chemistry at Gale. *Nature Communications*, *10*. https://doi.org/10.1038/s41467-019-12871-6

Gallagher, P.K. (1982). Applications of evolved gas analysis to the study of inorganic materials and processes. *Journal of Thermal Analysis*, *25*, 7–20.

Gates, W. P., Slade, P.G., Manceau, A., & Lanson, B. (2002). Site occupancies by iron in nontronites. *Clays and Clay Minerals*, *50*, 223–239.

Heller-Kallai, L., & Rozenson, I. (1980). Dehydroxylation of dioctahedral phyllosilicates. *Clays and Clay Minerals*, *28*, 355–368. https://doi.org/10.1346/Ccmn.1980.0280505

Hurowitz, J.A., & McLennan, S.M. (2006). A ~3.5 Ga record of water-limited, acidic weathering conditions on Mars. *Earth and Planetary Science Letters*, *260*, 432–443.

Jones, B.F., & Weir, A.H. (1983). Clay minerals of Lake Abert, an alkaline, saline lake. *Clays and Clay Minerals*, *31*, 161–172.

Kloprogge, J. T., Booy, E., Jansen, J.B.H., & Geus, J.W. (1994). The effect of thermal treatment on the properties of hydroxy-Al and hydroxy-Ga pillared montmorillonite and beidellite. *Clay Minerals*, *29*, 153–167.

Kokaly, R.F., Clark, R.N., Swayze, G.A., Livo, K.E., Hoefen, T.M., Pearson, N.C., Wise, R.A., Benzel, W.M., Lowers, H.A., Driscoll, R.L., and Klein, A.J. (2017). USGS Spectral Library Version 7: U.S. Geological Survey Data Series 1035, 61 p. https://doi.org/10.3133/ds1035

Léveillé, R. J., Bridges, J., Wiens, R.C., Mangold, N., Cousin, A., Lanza, N., and 15 co-authors (2014). Chemistry of fracture-filling raised ridges in Yellowknife Bay, Gale crater: window into past aqueous activity and habitability on Mars. *Journal of Geophysical Research – Planets*, *119*, 2398–2415. https://doi.org/10.1002/2014JE004620

Lynn, W.C., & Whittig, L.D. (1966). Alternation and formation of clay minerals during cat clay development. *Clays and Clay Minerals*, *14*, 241–248.

Mangold, N., E. Dehouck, C. Fedo, O. Forni, C. Achilles, T. Bristow, and 15 co-authors (2019). Chemical alteration of fine-grained sedimentary rocks at Gale crater. *Icarus*, *321*, 619–631. https://doi.org/10.1016/j.icarus.2018.11.004

Mahaffy, P.R., Webster, C.R., Cabane, M., Conrad, P.G., Coll, P., Atreya, S.K., Arvey, R., Bariciniak, M., Benna, M., Bleacher, L., Brinckerhoff, W.B., Eigenbrode, J.L., Carignan, D., Cascia, M., Chalmers, R.A., Dworkin, J.P., Errigo, T., Everson, P., Franz, H., Farley, R., Feng, S., Frazier, G., Freissinet, C., Glavin, D.P., Harpold, D.N., Hawk, D., Holmes, V., Johnson, C.S., Jones, A., Jordan, P., Kellogg, J., Lewis, J., Lyness, E., Malespin, C.A., Martin, D.K., Maurer, J., McAdam, A.C., McLennan, D., Nolan, T.J., Noriega, M., Pavlov, A.A., Prats, B., Raaen, E., Sheinman, O., Sheppard, D., Smith, J., Stern, J.C., Tan, F., Trainer, M., Ming, D.W., Morris, R.V., Jones, J., Gundersen, C., Steele, A., Wray, J., Botta, O., Leshin, L.A., Owen, T., Battel, S., Jakosky, B. M., Manning, H., Squyres, S., Navarro-Gonzalez, McKay, C.P., Paulin, F., Sternberg, R., Buch A., Sorensen, P., Kline-Schoder, R., Soscia, D., Szopa, C., Teinturier, S., Baffes, C., Feldman, J., Flesch, G., Forouhar, S., Garcia, R., Keymeulen, D., Woodward, S., Block, B.P., Arnett, K., Miller, R., Edmonson, C., Gorevan, S., & Mumm, E. (2012). The sample analysis at Mars investigation and instrument suite. *Space Science Reviews*, *170*, 401–478.

McAdam, A.C., Sutter, B., Archer, P.D., Franz, H.B., Wong, G.M., Lewis, J.M.T, Eigenbrode, J.L., Stern, J.C., Knudson, C.A., Clark, J.V., Andrejkovicova Slavka Ming, D.W., Morris, R.V., Achilles, C.N., Rampe, E.B., Bristow, T.F., Navarro-Gonzalez, R., Mahaffy, P.R., Thompson, L.M., Gellert, R., Williams, A.J., House, C.H., & Johnson, S. (2020). Constraints on the mineralogy and geochemistry of the Vera Rubin ridge, Gale crater, Mars, from Mars Science Laboratory Sample Analysis at Mars Evolved Gas Analyses. *Journal of Geophysical Research: Planets*, *125*. https://doi.org/10.1029/2019JE006309

McLennan, S. M., Anderson, R.B., Bell, III, J.F., Bridges, C., Calef, III, F.J., Campbell, J.L., and 433 co-authors (2014). Elemental geochemistry of sedimentary rocks at Yellowknife Bay, Gale crater, Mars. *Science*, *343*. https://doi.org/10.1126/science.1244734

Meunier, A. (2005). *Clays*. Springer.

Mermut, A. R., & Faz Cano, A. (2001). Baseline studies of the Clay Minerals Society Source Clays: chemical analyses of major elements. *Clays and Clay Minerals*, *49*, 381–386.

Mermut, A. R., & Lagaly, G. (2001). Baseline studies of the Clay Minerals Society Source Clays: layer-charge determination and characteristics of those minerals containing 2:1 layers. *Clays and Clay Minerals*, *49*, 393–397.

Ming, D. W., Archer, Jr, P.D., Glavin, D.P., Eigenbrode, J.L., Franz, H.B., Sutter, B., and 433 co-authors (2014). Volatile and organic compositions of sedimentary rocks in Yellowknife Bay, Gale crater, Mars. *Science*, *343*. https://doi.org/10.1126/science.1245267

Moore, D.M., & Reynolds, R.C. Jr (1997). *X-ray Diffraction and the Identification and Analysis of Clay Minerals*, 2nd edn. Oxford University Press, New York.

Morrison, S. M., Blake, D.F., Bristow, T.F., Castle, N., Chipera, S.J., Craig, P.I., and 18 co-authors (2024). Expanded insights into martian mineralogy: updated analysis of Gale crater's mineral composition via CheMin crystal chemical investigations. *Minerals*, *14*, 773. https://doi.org/10.3390/min14080773

Muller, F., Drits, V., Plancon, A., & Robert, J.L. (2000). Structural transformation of 2:1 dioctahedral layer silicates during dehydroxylation-rehydroxylation reactions. *Clays and Clay Minerals*, *48*, 572–585. https://doi.org/10.1346/Ccmn.2000.0480510

Mustard, J.F., Murchie, S.L., Pelkey, S.M., Ehlmann, B.L., Milliken, R.E., Grant, J. A., Bibring, J.-P., Poulet, F., Bishop, J., Noe Dobrea, E., Roach, L., Seelos, F., Arvidson, R.E., Wiseman, S., Green, R., Hash, C., Humm, D., Malaret, E., McGovern, J.A., Seelos, K., Clancy, T., Clark, R., Des Marais, D., Izenberg, N., Knudson, A., Langevin, Y., Martin, T., McGuire, P., Morris, R., Robinson, M., Roush, T., Smith, M., Swayze, G., Taylor, H., Titus, T., & Wolff, M. (2008). Hydrated silicate minerals on Mars observed by the Mars Reconnaissance Orbiter CRISM instrument. *Nature*, *454*, 305–309.

Pandey, A., Rampe, E.B., Ming, D.W., Deng, Y., Bedford, C.C., & Schwab, P. (2023). Quantification of amorphous Si, Al, and Fe in palagonitic Mars analogs by chemical extraction and X-ray spectroscopy. *Icarus*, *392*. https://doi.org/10.1016/j.icarus.2022.115362.

Poulet, F., Bibring, J.-P., Mustard, J.F., Gendrin, A., Mangold, N., Langevin, Y., Arvidson, R.E., Gondet, B., Gomez, C., & The Omega Team (2005). Phyllosilicates on Mars and implications for early martian climate. *Nature*, *438*, 623–627.

Rampe, E. B., Ming, D.W., Blake, D.F., Bristow, T.F., Chipera, S.J., Grotzinger, J. P., and 28 co-authors (2017). Mineralogy of an ancient lacustrine mudstone succession from the Murray formation, Gale crater, Mars. *Earth and Planetary Science Letters*, *471*, 172–185. https://doi.org/10.1016/j.epsl.2017.04.021

Rampe, E.B., Blake, D.F., Bristow, T.F., Ming, D.W., Vaniman, D.T., Morris, R. V., Achilles, C.N., Chipera, S.J., Morrison, S.M., Tu, V.M., Yen, A.S., Castle, N., Downs, G.W., Downs, R.T., Grotzinger, J.P., Hazen, R.M., Treiman, A.H., Peretyazhko, T.S., Des, Marais, D.J., Walroth, R.C., Craig, P.I., Cirsp, J.A., Lafuente, B., Morookian, J.M., Sarrazin, P.C., Thorpe, M.T., Bridges, J.C., Edgar, L.A., Fedo, C.M., Freissinet, C., Gellert, R., Mahaffy, P.R., Newsom, H. E., Johnson, J.R., Kah, L.C., Siebach, K.L., Schieber, J., Sun, V.Z., Vasavada, A. R., Wellington, D., Wiens, R.C. & **the MSL Science Team** (2020a). Mineralogy and geochemistry of sedimentary rocks and eolian sediments in Gale crater, Mars: a review after six Earth years of exploration with *Curiosity*. *Geochemistry*, *80*, 125605.

Rampe, E. B., T. F. Bristow, R. V. Morris, S. M. Morrison, C. N. Achilles, D. W. Ming, and 24 co-authors (2020b). Mineralogy of Vera Rubin ridge from the Mars Science Laboratory CheMin instrument. *Journal of Geophysical Research: Planets*, *125*. https://doi.org/10.1029/2019JE006306

Rossman, G., & Ehlmann, B. (2019). Electronic spectra of minerals in the visible and near-infrared regions. In Bishop, J., Bell III, J., & Moersch, J. (eds), *Remote Compositional Analysis: Techniques for Understanding Spectroscopy, Mineralogy, and Geochemistry of Planetary Surfaces* (Cambridge Planetary Science, pp. 3–20). Cambridge: Cambridge University Press. https://doi.10.1017/9781316888872.003

Rogers, A. D., & Christensen, P.R. (2007). Surface mineralogy of Martian low-albedo regions from MGS-TES data: implications for upper crustal evolution and surface alteration. *Journal of Geophysical Research*, *112*, E01003. https://doi.org/10.1029/2006JE002727

Sarrazin, P., Brunner, W., Blake, D., Gailhanou, M., Bish, D.L., Vaniman, D.T., and 6 co-authors (2008). Field studies of Mars analog materials using a portable XRD/XRF instrument. *LPS XXXIX*, abstract #1391.

Sheppard, R. Y., Milliken, R.E., Parente, M., & Itoh, Y. (2020). Updated perspectives and hypotheses on the mineralogy of lower Mt Sharp, as seen from orbit. *Journal of Geophysical Research: Planets*, *126*. https://doi.org/10.1029/2020JE006372

Thorpe, M.T., Bristow, T.F., Rampe, E.B., Tosca, N.J., Grotzinger, J.P., Bennett, K.A., Achilles, C.N., Blake, D.F., Chipera, S.J., Downs, G., Downs, R.T., Morrison, S.M., Tu, V., Castle, N., Craig, P., Des, Marais, D.J., Hazen, R. M., Ming, D.W., Morris, R.V., Treiman, A.H., Vaniman, D.T., Yen, A.S., Vasavada, A.R., Dehouck, E., Bridges, J.C., Berger, J., McAdam, A., Peretyazhko, T., Siebach, K.L., Byrk, A.B., Fox, V.K. & Fedo, C.M. (2022). Mars Science Laboratory CheMin data form the Glen Torridon region and the significance of lake-groundwater interactions in interpreting mineralogy and sedimentary history. *Journal of Geophysical Research: Planets*, *127*. https://doi.org/10.1029/2021JE007099

Tosca, N. J., & McLennan, S.M. (2006). Chemical divides and evaporite assemblages on Mars. *Earth and Planetary Science Letters*, *241*, 21–31. https://doi.org/10.1016/j.epsl.2005.10.021

Treiman, A.H., Morris, R.V., Agresti, D.G., Graff, T.G., Achilles, C.N., Rampe, E. B., Bristow, T.F., Ming, D.W., Blake, D.F., Vaniman, D.T., Bish, D.L., Chipera, S.J., Morrison, S.M., & Downs, R.T. (2014). Ferrian saponite from the Santa Monica Mountains (California, U.S.A., Earth): characterization as an analog for clay minerals on Mars with application to Yellowknife Bay in Gale Crater. *American Mineralogist*, *99*, 2234–2250.

Tu, V. M., Rampe, E.B., Bristow, T.F., Thorpe, M.T., Clark, J.V., Castle, N., and 27 co-authors (2021). A review of the phyllosilicates in Gale crater as detected by the CheMin instrument on the Mars Science Laboratory, Curiosity rover. *Minerals*, *11*. https://doi.org/10.3390/min11080847

Vaniman, D.T., Bish, D.L., Ming, D.W., Bristow, T.F., Morris, R.V., Blake, D.F., Chipera, S.J., Treiman, A.H., Rampe, E.B., Rice, M., Achilles, CN., Grotzinger, J.P., McLennan, S.M., Williams, J., Bell, III, J.F., Newsom, H. E., Downs, R.T., Maurice, S., Sarrazin, P., Yen, A.S., Morookian, J.M., Farmer, J.D., Stack, K., Milliken, R.E., Ehlmann, B.L., Sumner, D.Y., Berger, G., Crisp, J.A., Hurowitz, J.A., Anderson, R., Des, Marais, D.J., Stolper, E.M., Edgett, K.S., Gupta, S., Spanovich, N., and the MSL Science Team (2014). Mineralogy of a mudstone at Yellowknife Bay, Gale crater, Mars. *Science*, *343*, 1243480.

Vicente, M. A., M. A. Bañares-Muñoz, M. Suárez, J. M. Pozas, J. D. López-González, J. Santamaría, & A. Jiménez-López (1996). *Langmuir*, *12*, 5143–5147.

Vicente, M.A., Suarez, M., Bañares-Muñoz, M.A., & Martin-Pozas, J. (1997). Characterization of solids obtained by pillaring of Griffithite (high iron content saponite) with Al-oligomers. *Clays and Clay Minerals*, *45*, 761–768.

Weaver, C.E. (1989). *Clays, Muds, and Shales*. Elsevier.

Wiens, R. C., Maurice, S., Robinson, S.H., Nelson, A.E., Cais, P., Bernardi, P., and 126 co-authors (2021). The SuperCam instrument suite on the NASA Mars 2020 rover: body unit and combined system tests. *Space Science Reviews*, *21*, 4. https://doi.org/10.1007/s11214-020-00777-5

Xeidakis, G.S. (1996). Stabilization of swelling clays by $Mg(OH)_2$. Factors affecting hydroxy-Mg-interlaying in swelling clays. *Engineering Geology*, *44*, 96–103.